1 **Oxidation pathways and emission sources of atmospheric particulate nitrate in Seoul:**

2 **based on δ^{15}N and Δ^{17}O of PM$_{2.5}$**

4 Saehee Lim[a], Meehye Lee[a,*], Joel Savarino[b], and Paolo Laj[b]

5 [a] Dept. of Earth and Environmental Sciences, Korea University, Seoul, 02841, South Korea

6 [b] Univ. Grenoble-Alpes, CNRS, IRD, Grenoble INP, Institute for Geosciences and Environmental

7 Research (IGE), Grenoble, 38000, France

9 *Correspondence to: M. Lee (meehye@korea.ac.kr)

11 **Abstract**

12 PM$_{2.5}$ haze pollution driven by secondary inorganic NO$_3^-$ has been a great concern in East Asia. It is,

13 therefore, imperative to identify its sources and oxidation processes, for which nitrogen and oxygen

14 stable isotopes are powerful tracers. Here, we determined the δ^{15}N (NO$_3^-$) and Δ^{17}O (NO$_3^-$) of PM$_{2.5}$ in

15 Seoul during the summer of 2018 and the winter of 2018-2019, and estimated quantitatively the relative

16 contribution of oxidation pathways for particulate NO$_3^-$ and investigated major NO$_x$ emission sources.

17 In the range of PM$_{2.5}$ mass concentration from 7.5 μg m^{-3} (summer) to 139.0 μg m^{-3} (winter), the mean

18 δ^{15}N was -0.7 ± 3.3 ‰ and 3.8 ± 3.7 ‰, and the mean Δ^{17}O was 23.2 ± 2.2 ‰ and 27.7 ± 2.2 ‰ in the

19 summer and winter, respectively. While OH oxidation was the dominant pathway for NO$_3^-$ during the

20 summer (87 %), nighttime formation via N$_2$O$_5$ and NO$_3$ was more important (38 %) during the winter,

21 when aerosol liquid water content (AWLC) and nitrogen oxidation ratio (NOR) were higher.

22 Interestingly, the highest Δ^{17}O was coupled with the lowest δ^{15}N and highest NOR during the record-

23 breaking winter PM$_{2.5}$ episodes, revealing the critical role of photochemical oxidation process in severe

24 winter haze development. For NOx sources, atmospheric δ^{15}N (NO$_x$) estimated from measured δ^{15}N

25 (NO$_3^-$) considering isotope fractionation effects indicates vehicle emissions as the most important

26 emission source of NO$_x$ in Seoul. The contribution from biogenic soil and coal combustion was slightly

27 increased in summer and winter, respectively. Our results built on multiple-isotope approach provide

28 the first explicit evidence for NO$_3^-$ formation processes and major NO$_x$ emission sources in Seoul

29   megacity and suggest an effective mitigation measure to improve $PM_{2.5}$ pollutions.

30   **Keywords**: nitrate, NO_x, oxidation processes, emission sources, $PM_{2.5}$ haze, triple oxygen isotope,
31   nitrogen stable isotope

1. Introduction

35   In Northeast Asia, air pollution characterized by high $PM_{2.5}$ (particulate matters with aerodynamic
36   diameter smaller than 2.5 μm) and ozone concentrations has received significant attention due to its
37   serious effects on human health (Lelieveld et al., 2015; Xie et al., 2019). As a result of extensive efforts
38   by East Asian countries to improve the ambient air quality, anthropogenic emissions of SO_x, NO_x, and
39   CO has been significantly reduced, particularly in China (Cheng et al., 2019). Nonetheless, the number
40   of severe haze events and the duration have been increased, which is not understood clearly.

41   It is also noteworthy that there are common chemical and meteorological characteristics in the
42   occurrence of the $PM_{2.5}$ haze pollution in northeast Asia, such as inorganic species-dominated chemical
43   composition (Liu et al., 2018; Shao et al., 2018; Wang et al., 2019a) and transboundary transport of
44   haze aerosol depending on the synoptic atmospheric circulation (Quan et al., 2020; Shi et al., 2020;
45   Zheng et al., 2019). Overall, approximately 40% of $PM_{2.5}$ consists of NO_3^-, SO_4^{2-}, and NH_4^+ (secondary
46   inorganic aerosol, "SIA") in both urban and background sites in China (Liu et al., 2018) for the period
47   of 2012-2013. The mass contribution of SIA was further augmented up to 69% at urban Beijing and
48   island sites (Changdao) in North China Plain ("NCP") during the 2016 spring (Lim et al., 2020). A large
49   increase in SIA mass is particularly associated with efficient formation of NO_3^- in cold months (most
50   frequently in Dec. to Mar.), leading to a rapid increase in $PM_{2.5}$ concentration and developing a
51   persistent haze pollution on a regional scale (Li et al., 2018; Xu et al., 2019). Recent studies suggest
52   that the regional occurrence of the $PM_{2.5}$ haze events derived by NO_3^- across Asian continent has been
53   associated with long-range transport of air pollutants promoted by cold fronts and their intrusion in
54   downward regions by the development of the atmospheric boundary layer (Kang et al., 2019; Lee et al.,
55   2019). However, scientific understanding is still limited because the rapid increase of $PM_{2.5}$ NO_3^- is the
56   result of complex interplay of oxidation and transformation mechanisms producing NO_3^- from various
57   fossil and non-fossil sources of NO_x with micro-to-synoptic meteorology creating the conditions for
58   NO_3^- formation. In addition, considering that NO_x emissions from bottom-up emission inventory are

59   smaller than top-down estimates by satellites (e.g.,Goldberg et al., 2019), our understanding of NO_x

60   emissions is poor.

61   In order to better understand processes of NO_3^- formation including NO_x emission sources in East Asia,

62   a growing number of recent studies have suggested nitrogen and oxygen stable isotope-based

63   measurement as a robust and useful tool for providing important clues for NO_3^- formation as well as

64   NO_x emission sources (He et al., 2018; Lim et al., 2019, 2020; Song et al., 2019; Zong et al., 2017,

65   2020). The isotopic composition is expressed in parts per thousand (‰) and reported as δ (‰)

66     $=(R_{sample}/R_{standard}-1)\times 1000$ with R being the ratio of the heavy isotope over the light isotope (e.g., $^{15}N/^{14}N$,

67     $^{18}O/^{16}O$, $^{17}O/^{16}O$) in a sample (R_{sample}) and in the international standard ($R_{standard}$). The international

68   standards are the Vienna Standard Mean Ocean Water, VSMOW and atmospheric N_2 for oxygen and

69   nitrogen ratios, respectively. In terms of NO_x emission sources, the major NO_x sources are distinguished

70   in their nitrogen isotopic compositions; biogenic soil (driven by fertilizer use; -35.1‰ ± 10.2‰) (Felix

71   and Elliott, 2014; Li and Wang, 2008; Yu and Elliott, 2017), biomass burning (1.8‰ ±1.8‰) (Fibiger

72   and Hastings, 2016), vehicle emissions (-2.5‰ ± 1.5‰) (Walters et al., 2015), and coal combustion

73   (14.2‰ ± 4.5‰) (Felix et al., 2012; Heaton, 1990). Despite evidences that $\delta^{15}N$ (NO_x) can serve as a

74   useful tracer of NO_x emission sources, during NO_y photochemical cycling and its loss processes, the

75     $\delta^{15}N$ of initial NO_x can be significantly altered by both kinetic and equilibrium isotopic fractionation

76   effects (ε_N), complicating the link between $\delta^{15}N$ (NO_3^-) and $\delta^{15}N$ (NO_x) (Freyer et al., 1993; Li et al.,

77   2020).

78

79   The formation processes of HNO_3 in the atmosphere consist of $NO-NO_2$ photochemical cycle (R1-R3)

80   and post NO_2 oxidation reactions (R4-R8). During the NO_x cycling, nitrogen isotopic fractionation is

81   affected by unidirectional reactions of Leighton cycle and NO_x isotope exchange equilibrium. A recent

82   laboratory experiment has shown that the Leighton cycle isotope effect (LCIE) associated solely with

83   O_3 reaction (R1) and equilibrium isotopic effect (EIE) were -10 ‰ and 28.9 ‰ at room temperature,

84   respectively (Li et al., 2020). The relative importance of these two effects on $\delta^{15}N$ (NO_2) also depends

85   on NO_x levels, leading to increase (decrease) in $\delta^{15}N$ (NO_2) relative to $\delta^{15}N$ (NO_x) values at high (low)

86   NO_x conditions (Kamezaki et al., 2019; Li et al., 2020; Walters et al., 2018). Overall, the nitrogen

87   isotope exchange equilibrium has been suggested to be the dominant fractionation process in $NO-NO_2$

88   cycling at urban atmosphere (Freyer et al., 1993) and oxidation reactions forming nitric acid (HNO_3)

89   and particulate NO_3^- (Savarino et al., 2013).

90      $NO + O_3 \rightarrow NO_2 + O_2$ (R1)

91      $NO + RO_2 (HO_2) \rightarrow NO_2 + RO (OH)$ (R2)

92      $NO_2 + h\nu \rightarrow NO + O(^3P)$ (R3)

93      $NO_2 + OH \rightarrow HNO_3 (g)$ (R4)

94      $NO_2 + O_3 \rightarrow NO_3 + O_2$ (R5)

95      $NO_2 + NO_3 + M \leftrightarrow N_2O_5$ (R6)

96      $N_2O_5 + H_2O \xrightarrow{aerosol} 2HNO_3 (aq)$ (R7)

97      $NO_3 + RH \rightarrow HNO_3 (g) + R$ (R8)

98   The kinetic fractionation effect during daytime oxidation of NO_2 to HNO_3 (R4) is relatively minor,

99   being estimated to be -3‰ (Freyer, 1991). During the nighttime when most NO is oxidized to NO_2

100   without NO_x photolysis, the isotopic equilibrium between NO_2, NO_3, and N_2O_5 should be achieved (R6).

101   The nighttime thermal equilibrium likely favors the partitioning of ^{15}N into N_2O_5 relative to NO_2 and

102   consequently induces a large isotopic fractionation effect of 25.5‰ (Walters and Michalski, 2015, R5-

103   R6). On the other hand, the nitrogen partitioning between NO_2 and NO_3 (R5) may induces a

104   fractionation effect of about -18‰ (Walters and Michalski, 2015). These N isotope fractionation effects

105   should be first evaluated to explore NO_x source contributions, which should be based on combining

106   with a robust tracer for the contributions of NO_3^- oxidation pathways.

107   Lately, $\Delta^{17}O$ (NO_3^-) has been used for tracing NO_3^- oxidation pathways (Alexander et al., 2009, 2020;

108   Morin et al., 2009; Savarino et al., 2007, 2013). Earlier researches observed atmospheric NO_3^- is

109   anomalously enriched in ^{17}O (Michalski et al., 2003), which stems from O_3 formation reactions, where

110   a rare isotope effect leads to excess ^{17}O enrichment relative to what is expected based on the ^{18}O

111   enrichments (Thiemens, 1999, 2006)(Thiemens, 2006). This enrichment is quantified by $\Delta^{17}O$ notation

112   (^{17}O-excess, defined as $\delta^{17}O - 0.52 \times \delta^{18}O$). Since non-zero $\Delta^{17}O$ strictly reflects a photochemical effect,

113   NO_3^- produced by denitrification in soils should have $\Delta^{17}O$ of zero. The mass-independent $\Delta^{17}O$

114   signature of O_3 is transferred to NO_x, in which the number of oxygen atom from O_3 is involved in NO_x.

115   In this way, the $\Delta^{17}O$ (NO_3^-) is served as a conservative marker to track the chemical formation of

116   atmospheric NO_3^-. Photochemical formation by peroxy radicals (HO_2 and RO_2) leads to a relatively low

117     $\Delta^{17}O$ (NO_3^-), whereas nighttime formation through N_2O_5 and NO_3 results in high $\Delta^{17}O$ (Michalski et al.,

118   2003; Morin et al., 2009; Savarino et al., 2007). Consequently, the difference in $\Delta^{17}O$ (NO_3^-) suggests

119   approaching a proportional contribution of daytime and nighttime oxidation of NO_3^-.

120 To date, few field studies have coupled $\Delta^{17}O$ (NO_3^-) and $\delta^{15}N$ (NO_3^-) to investigate NO_x-to-NO_3^-

121 oxidation processes and emission sources of NO_x, e.g., field researches in Japan (Nelson et al., 2018),

122 west Virginia USA (Rose et al., 2019), Shanghai , China (He et al., 2020) and Beijing, China (He et al.,

123 2018; Song et al., 2020).

124 In this study, we present the measurement results of $\delta^{15}N$ and $\Delta^{17}O$ of NO_3^- in Seoul during the summer

125 of 2018 and the winter of 2018-2019, when we encountered the record-breaking $PM_{2.5}$ concentrations.

126 Then, the $\delta^{15}N$ and $\Delta^{17}O$ measurements are used to evaluate seasonally distinct atmospheric oxidation

127 pathways of NO_3^- and to explore major NO_x source contributions in the study region.

128

2. Measurements and methods

2.1. Sampling

131 We collected $PM_{2.5}$ filter samples on the rooftop of six-story Asan science building at Korea University

132 campus located in northeast Seoul, the capital of South Korea (37.59° N, 127.02° E; Figure 1) during

133 the summer 2018 (26 May to 22 Aug.; n = 13) and the winter 2018-2019 (27 Dec. to 8 Mar.; n = 18).

134 Seoul is a metropolitan area with a population of 9.77 million and known to be influenced by heavy

135 road traffic all around. The $PM_{2.5}$ particulates were collected on quartz filters (20 cm x 25 cm ; Pallflex

136 Products, Putnam, USA) at a nominal flow rate of 96 m^3 hr^{-1} for 1 to 3 days using a high-volume air

137 sampler (3000 series, Ecotech, Australia). Filters were analyzed for water-soluble ions, carbonaceous

138 compounds, total nitrogen (TN) and carbon (TC), and stable nitrogen and oxygen isotopic ratios.

139 Reactive gases including O_3, NO, NO_2, SO_2, and CO, and meteorological suite including air temperature,

140 relative humidity, and wind speed and direction were measured hourly at the campus and nearby

141 monitoring sites run by the National Institute of Environmental Research (NIER) and the Korea

142 Meteorological Administration (KAM), respectively. These data were averaged daily for comparison

143 with filter-based chemical composition data, if necessary.

144

2.2. Chemical analyses

146 Filters were stored in a freezer pending chemical analysis. Chemical composition of $PM_{2.5}$ was

147 determined for 8 water-soluble ions (Cl^-, NO_3^-, SO_4^{2-}, Na^+, NH_4^+, K^+, Ca^{2+}, and Mg^{2+}) by ion

148 chromatography (IC; Eco-IC, Metrohm, Switzerland); OC and EC by an OC-EC analyzer (Sunset

Laboratory Inc., US) using the thermo-optical transmittance method (NIOSH870); and TC and total nitrogen (TN) by an elemental analyzer (EA, Fisons NA-1500NC, Thermo, Waltham, MA, USA). Mass concentrations of these constituents were corrected for laboratory and field blanks. The detection limit, determined as three standard deviations (SD) above blank concentrations, was <0.1 ppm for ionic species, 0.5 $\mu g\ cm^{-3}$ for TC (the sum of OC and EC), and 0.8g μgN and 0.5 μgC per punched filter area for TN and TC, respectively. Details of the analytical methods can be found elsewhere (Lim et al., 2020).

Following the bacterial denitrifier method (Casciotti et al., 2002; McIlvin and Casciotti, 2011), the $\Delta^{17}O$ of NO_3^- was measured simultaneously with $\delta^{18}O$ and $\delta^{15}N$ coupled with an IRMS measurement using an in-house peripheral system at the Université Grenoble Alpes (Morin et al., 2009). In brief, NO_3^- of samples was converted to N_2O via bacterial denitrification and the N_2O was further converted into O_2 and N_2, which were separated via a gas chromatography column before being introduced to the IRMS system (Thermo Finnigan MAT 253 Isotope Ratio Mass Spectrometer). Samples were measured in batch with reference materials following strictly the identical treatment principles, including the same water matrix for standards and samples. Together with samples, a subset of international nitrate reference materials (US Geological Survey 32, 34, and 35, as well as their mixtures) was measured for correction and calibration of $\Delta^{17}O$ and $\delta^{18}O$ values relative to VSMOW and $\delta^{15}N$ values relative to air N_2. The overall accuracy of the method is estimated as the reduced standard deviation of the residuals from the linear regression between the measured reference materials and their expected values (Morin et al., 2009). For these sets of analyses, the obtained uncertainties values (1σ) were 0.4 ‰ and 0.3 ‰ for $\Delta^{17}O$ (NO_3^-) and $\delta^{15}N$ (NO_3^-), respectively. The analytical procedure used in this study strictly followed the method described in Morin et al. (2009) which adheres to the now standard bacterial method coupled with the gold catalyst for the thermal decomposition of N_2O into N_2 and O_2 (Kaiser et al., 2007).

2.3. Quantifying isotope fractionation effects

2.3.1. Isotope fractionation effects of NO_2 oxidation to atmospheric particulate NO_3^- : $\delta^{15}N$ (NO_3^-)

The HNO_3 forms through three major pathways including (i) OH pathway, (ii) O_3 pathway associated with N_2O_5, and (iii) O_3 pathway associated with NO_3.

 OH pathway

When NO and NO_2 coexist in similar quantities due to the Leighton cycle, ^{15}N is preferentially partitioned into NO_2 via the equilibrium isotope effect, leading to higher $\delta^{15}N$ in NO_2 relative to NO and NO_x (Freyer et al., 1993; Walters et al., 2016). Considering the comparable concentrations of NO and NO_2 over a year in Seoul (Figure S1 and S1), the N isotope effects on $\delta^{15}N$ (NO_3^-) should be significantly affected by NO_x photochemical interactions. The relative importance of EIE and LCIE to $\delta^{15}N(NO_2)$ can be assessed by comparing lifetimes of NO_2 with respect to isotope exchange with NO ($\tau_{exchange}$) and photolysis (τ_{NO2+hv}). In this regard, the "A" factor was defined as $\tau_{exchange}/\tau_{NO2+hv} = j_{NO2}/k_1 \times [NO]$ ($k_1 = 8.14 \times 10^{-14}$ cm^3 s^{-1}, Sharma et al., 1970) by Li et al. (2020, 2021). These studies demonstrated that A was as small as 0.01-0.5 in EIE-dominated regime with $NO_x > 20$ ppbv and the ratio of $NO_2/NO_x < 0.6$. In Seoul, to simply evaluate the relative importance of EIE and LCIE only (not for ^{15}N correction), A factor was estimated to be 0.08 ± 0.20 (median ± standard deviation) and 0.60 ± 0.51 during the winter and summer months, respectively, indicating the significant influence of the equilibrium isotope effect on NO-NO_2 isotopic fractionation. The time series j_{NO2} was calculated using the Master Chemical Mechanisms (MCM) (Saunders et al., 2003) model.

After photochemical NO_x photochemical cycling, NO_2 is oxidized by the reaction with OH radical to form atmospheric HNO_3 ("HNO_3 (R4) pathway"). The N fractionation effect of particulate NO_3^- produced via HNO_3 (R4) pathway (ε_1, unit in ‰) can be expressed as the following, neglecting kinetic isotope effects associated with HNO_3 (R4) pathway (Walters and Michalski, 2016):

$$\delta^{15}N \ (HNO_3) \ (R4) = \delta^{15}N \ (NO_2) = \delta^{15}N \ (NO_x) + \varepsilon_1 \tag{Eq. 1-1}$$

$$\varepsilon_1 = ((^{15}\alpha_{NO2/NO} - 1) \ (1 - f_{NO2})) / ((1 - f_{NO2}) + (^{15}\alpha_{NO2/NO} \times f_{NO2})) \tag{Eq. 1-2}$$

, where f_{NO2} is the fraction of NO_2 relative to the total NO_x, and $^{15}\alpha_{NO2/NO}$ is the temperature-dependent isotope equilibrium exchange fractionation factor for NO_2/NO (Walters et al., 2016). In the present study, the measured f_{NO2} was used individually for summer samples and a seasonal mean f_{NO2} (0.69) was applied to winter samples due to the lack of availability of continuous NO-NO_2 measurement data.

Oxidation of NO_x to HNO_3 is regarded as the formation pathway of particulate NO_3^- via the "HNO_3 (R4) pathway" due to the unconstrained isotope fractionation effect between HNO_3 and NO_3^-, resulting in the following equation:

207     $\delta^{15}N$ (HNO$_3$) (R4) = $\delta^{15}N$ (NO$_3^-$) (R4)   (Eq. 1-3)

208

O$_3$ pathways associated with N$_2$O$_5$, and NO$_3$.

210   During the nighttime when NO is oxidized into NO$_2$ without photolyzing back to NO and fresh

211   emissions of NO is negligible, NO$_x$ exists almost as NO$_2$ and thus, $\delta^{15}N$ (NO$_2$) should be reflective of

212   the $\delta^{15}N$ of NO$_x$ sources. If NO$_2$ is oxidized to N$_2$O$_5$, the isotopic equilibrium is likely to be achieved

213   between NO$_2$, NO$_3$, and N$_2$O$_5$ by chemical equilibrium (R6) and the $\delta^{15}N$ values of N$_2$O$_5$ and NO$_3$ will

214   reflect the isotope equilibrium fractionation factors relative to NO$_2$ (i.e., $^{15}\alpha_{N2O5/NO2}$ and $^{15}\alpha_{NO3/NO2}$,

215   values were adopted from supplementary Table S5 in Walters and Michalski, 2016). Finally, $\delta^{15}N$ of

216   particulate NO$_3^-$ produced from dark pathways can be expressed as the following, neglecting currently

217   unconstrained kinetic isotopic fractionation associated with R7 and R8 (Walters and Michalski, 2016).

218

219     $\delta^{15}N$ (HNO$_3$) (R7) = $\delta^{15}N$ (N$_2$O$_5$) = $\delta^{15}N$ (NO$_2$) + ε_2 (Eq. 2-1)

220   ε_2 = ($^{15}\alpha_{N2O5/NO2}$ - 1)   (Eq. 2-2)

221     $\delta^{15}N$ (HNO$_3$) (R7) = $\delta^{15}N$ (NO$_3^-$) (R7)   (Eq. 2-3)

222     $\delta^{15}N$ (HNO$_3$) (R8) = $\delta^{15}N$ (NO$_3$) = $\delta^{15}N$ (NO$_2$) + ε_3 (Eq. 3-1)

223   ε_3 = ($^{15}\alpha_{NO3/NO2}$ - 1)   (Eq. 3-2)

224     $\delta^{15}N$ (HNO$_3$) (R8) = $\delta^{15}N$ (NO$_3^-$) (R8)   (Eq. 3-3)

225

226   Therefore, the $\delta^{15}N$ (NO$_x$) in the atmosphere can be expressed using measured $\delta^{15}N$ (NO$_3^-$) and the net

227   N isotope fractionation effect, ε_N.

228     $\delta^{15}N$ (NO$_x$)$_{atmosphere}$ = $\delta^{15}N$ (NO$_3^-$) $_{measured}$ - ε_N (Eq. 4-1)

229   ε_N = $\varepsilon_1 \times f_1 + \varepsilon_2 \times f_2 + \varepsilon_3 \times f_3$ (Eq. 4-2)

230   , where ε_1, ε_2, and ε_3 are abovementioned N isotope fractionation effect of pathways (i), (ii), and (iii),

231   respectively, and the proportional contributions (f_1, f_2, and f_3) of the three NO$_3^-$ formation pathways

232   were estimated from $\Delta^{17}O$ measurements (Sect. 2.3.2).

233

234   **2.3.2. Proportional contributions of three formation pathways to atmospheric particulate**
235   **NO_3^-: $\Delta^{17}O$ (NO_3^-)**

236   Due to its mass-independent nature, $\Delta^{17}O$ of particulate NO_3^- is a conservative tracer of photochemical
237   NO_3^- formation (Michalski et al., 2003, 2004). At photochemical steady state, the $\Delta^{17}O$ of NO_2 is
238   determined by the relative production rate of NO_2 via O_3 oxidation (R1) in NO_2 production (R1 and R2)
239   (f_{O3}) and the mass-independent $\Delta^{17}O$ anomaly transferred from O_3 during R1 ($\Delta^{17}O\text{-}O_3^*$):

240    $\Delta^{17}O$ (NO_2) (‰) $= f_{O3} \times \Delta^{17}O\text{-}O_3^*$ (Eq. 5)

241   f_{O3} was adopted from a previous study conducted in Beijing (Wang et al., 2019b), where the seasonal
242   mean was 0.858 and 0.918 for summer and winter, respectively. $\Delta^{17}O\text{-}O_3^*$ can be approximated as 1.5
243    $\times \Delta^{17}O\text{-}O_3$ because of the isotopic asymmetry of O_3 (Michalski and Bhattacharya, 2009). In this study,
244   the $\Delta^{17}O\text{-}O_3^*$ is 37.5 ± 2.2‰ (mean ± SD) averaged from literature sources as the isotopic composition
245   of ozone shows a remarkable stability in the lower troposphere (Ishino et al., 2017; Vicars et al., 2012;
246   Vicars and Savarino, 2014)

247   The $\Delta^{17}O$ of particulate NO_3^- produced via the three formation pathways can be predicted by distinct
248    $\Delta^{17}O$ transfer functions as the following (Morin et al., 2011):

249    $\Delta^{17}O$ (NO_3^-) (1) (‰) $= 2/3\ \Delta^{17}O(NO_2) = 2/3\ f_{O3} \times \Delta^{17}O\text{-}O_3^*$ (Eq. 6-1)

250    $\Delta^{17}O$ (NO_3^-) (2) (‰) $= 5/6\ \Delta^{17}O(N_2O_5) = 1/3\ \Delta^{17}O(NO2) + 1/2\ \Delta^{17}O(NO_3) = 1/6\ \Delta^{17}O\text{-}O_3^*\ (4\,f_{O3} +1)$

251   (Eq. 6-2)

252    $\Delta^{17}O$ (NO_3^-) (3) (‰) $= \Delta^{17}O(NO_3) = 2/3\ \Delta^{17}O(NO_2) +1/3\ \Delta^{17}O\text{-}O_3^* =1/3\ \Delta^{17}O\text{-}O_3^*\ (2\,f_{O3} +1)$ (Eq. 6-3)

253   Finally, the $\Delta^{17}O$ (NO_3^-) can be expressed as the following:

254    $\Delta^{17}O$ (NO_3^-)$_{measured} = \Delta^{17}O$ (NO_3^-) (R4) $\times f_1 + \Delta^{17}O$ (NO_3^-) (R7) $\times f_2 + \Delta^{17}O$ (NO_3^-) (R8) $\times f_3$
255   (Eq. 7)

256 where $\Delta^{17}O$ $(NO_3^-)_{measured}$ is the measured value in this study and the three endmember values of $\Delta^{17}O$
257 (NO_3^-) (R4), $\Delta^{17}O$ (NO_3^-) (R7), and $\Delta^{17}O$ (NO_3^-) (R8) are calculated using Eqs. (6-1 to 6-3). The
258 proportional contributions of the three NO_3^- formation pathways ($f_1 + f_2 + f_3 = 1$) were estimated by the
259 SIAR model (Sect. 2.5.) for the winter and the summer months.

2.4. Estimation of PM$_{2.5}$ Aerosol Liquid Water Content (ALWC) and aerosol pH

262 ISORROPIA-II is a thermodynamic equilibrium model for the Cl^-, NO_3^-, SO_4^{2-}, Na^+, NH_4^+, K^+, Ca^{2+},
263 Mg^{2+}, and H_2O aerosol system (Fountoukis and Nenes, 2007). In the present study, the model was run
264 as a "forward" and "metastable" mode to calculate aerosol liquid water content (ALWC) and pH. The
265 detailed information of the model is found in Fountoukis and Nenes (2007). As input parameters, the
266 concentrations of water-soluble ions that were measured by NIER and ambient RH and temperature
267 were used for the model.

2.5. Bayesian stable isotope mixing model (stable isotope analysis in R, SIAR)

270 For quantifying proportional contribution of three NO_3^- formation pathways (f_1, f_2, and f_3 in Eq. 4-2),
271 we used the Bayesian stable isotope mixing model (Parnell et al., 2013) implemented using the SIMMR
272 package in R software, which is available at https://cran.r-project.org/web/packages/simmr/index.html.
273 The Bayesian Markov Chain Monte Carlo approach is adequate to provide the relative contribution of
274 the endmembers. Detailed information of the SIAR can be found in Parnell et al. (2010). As input data,
275 measured $\Delta^{17}O$ (NO_3^-) and estimated $\Delta^{17}O$ (NO_3^-) endmember values of each pathway were treated in
276 SIAR model. Similar use of the SIAR model can be found elsewhere (Song et al., 2020; Wang et al.,
277 2019b).

2.6. Backward airmass trajectory

281 Two-day air mass backward trajectories were analyzed using the HYSPLIT (Hybrid Single-Particle
282 Lagrangian Integrated Trajectory) model with meteorological input from the global data assimilation
283 system (a regular 1° x 1° longitude-latitude grid) (Stein et al., 2015;

284 https://ready.arl.noaa.gov/HYSPLIT.php) . The trajectories were calculated every 6 h at an elevation of

285 500 m above sea level. The potential source contribution function (PSCF) was then applied to calculate

286 the probable source location (latitude i and longitude j), which is determined here as the ratio of the

287 number of trajectory end points associated with measured $\delta^{15}N$ (NO_3^-) values higher than a threshold

288 value (set to 95th percentile of $\delta^{15}N$ (NO_3^-) (m_{ij}) to the total number of points (n_{ij}) in the $i\,j$ th grid cell).

289 The PSCF calculation was made in the openair package, R software (https://cran.r-

290 project.org/web/packages/openair/index.html) (Carslaw and Ropkins, 2012).

291

3. Results and discussion

3.1. Seasonal characteristics of PM$_{2.5}$ concentration, $\delta^{15}N$ (NO_3^-), and $\Delta^{17}O$ (NO_3^-)

294 PM$_{2.5}$ mass concentration varied from 7.5 µg m^{-3} to 139.0 µg m^{-3} for the whole sampling period.

295 According to the typical synoptic weather patterns of East Asia (Kim et al., 2007), the measurements

296 are divided into summer (May-Aug) and winter (Oct.-Mar.) groups. A clear seasonal difference in PM$_{2.5}$

297 concentration and its composition were observed with significantly higher concentrations of mass and

298 inorganic constituent in the winter than in the summer (Table 1 and Figure S1).

299 During the summer, PM$_{2.5}$ concentration ranged from 7.5 µg m^{-3} to 34.5 µg m^{-3} with a mean of 22.7 $\pm$

300 6.9 µg m^{-3}. The mean concentration of TC and TN was 4.6 $\pm$ 1.4 µgC m^{-3} and 1.9 $\pm$ 1.0 µgN m^{-3},

301 respectively, resulting in the mean TC/TN ratio of 2.7 $\pm$ 2.0. The mass concentrations of all measured

302 species were much higher in the winter, during which PM$_{2.5}$ concentration was raised up to 139.0 µg m^{-3}

303 from 10.6 µg m^{-3} with a mean of 61.7 $\pm$ 39.2 µg m^{-3}. Accordingly, the mean of TC and TN was 15.2 $\pm$

304 4.5 µgC m^{-3} and 11.8 $\pm$ 7.7 µgN m^{-3}, respectively and the mean TC/TN ratio of 0.9 $\pm$ 0.7 was noticeably

305 lower than that of the summer.

306 For the entire experiment, the mean mass fraction against PM$_{2.5}$ was the highest for NO_3^- (26% $\pm$ 23%),

307 followed by SO_4^{2-} (20% $\pm$ 1%) and NH_4^+ (14% $\pm$ 1%), highlighting the contribution of SIA to PM$_{2.5}$

308 mass. The NO_3^- mass concentration varied from 0.2 µg m^{-3} to 69.3 µg m^{-3} with a mean of 17.6 $\pm$ 22.1

309 µg m^{-3}. Seasonally, the NO_3^- concentration was significantly higher in the winter (29.7 $\pm$ 22.1 µg m^{-3})

310 than summer (0.8 $\pm$ 0.9 µg m^{-3}). TN existed completely as inorganic N from both NO_3^- and NH_4^+ during

311 the winter (regression slope of 1.0). During the summer, NO_3^- and NH_4^+ comprised 67% of TN and the

312 rest (33 %) was assumed to be organic nitrogen (ON) components. In contrast, the mass fraction of

313   SO_4^{2-} against $PM_{2.5}$ was higher in the summer (23%) than winter (19%). The seasonal characteristics of

314   chemical composition implies the significant role of inorganic nitrogen species in $PM_{2.5}$ mass increase

315   in winter and ON and sulfate in summer.

316   Both $\delta^{15}N$ (NO_3^-) and $\Delta^{17}O$ (NO_3^-) exhibited an inverse correlation with ambient temperature (r= -0.87

317   and r= -0.55, respectively). The $\delta^{15}N$ (NO_3^-) exhibited higher values in winter with a weight-mean of -

318   0.7‰ ± 3.3 ‰ and 3.8‰ ± 3.7 ‰ in the summer and the winter, respectively. This seasonal pattern of

319      $\delta^{15}N$ (NO_3^-) has been typically observed in East Asia regions (Li et al., 2019; Song et al., 2019; Zong et

320   al., 2020). Analysis of backward airmass trajectory indicates that the lower and the upper bound of $\delta^{15}N$

321   (NO_3^-) were associated with air masses from the ocean by southerly and easterly winds in the summer

322   and from Siberia by northerly winds in winter, respectively (Figure S3). In comparison with urban China

323   (Figure 2a), averaged summer $\delta^{15}N$ (NO_3^-) values were comparable between Seoul and all urban

324   Chinese sites reported here, whereas in winter, $\delta^{15}N$ (NO_3^-) of Seoul was similar to those of Shanghai

325   and Guangzhou rather than $\delta^{15}N$ (NO_3^-) of Beijing that were higher than 10‰. Another observation at

326   a mountain station in Taiwan shows that the highest $\delta^{15}N$ (NO_3^-) was found in spring when the level of

327   anthropogenic constituents were elevated (Guha et al., 2017). These observations over East Asia may

328   suggest at some extent that the seasonal pattern of $\delta^{15}N$ (NO_3^-) is basically associated with synoptic

329   meteorological condition that controls the type and strength of emission sources, where low and high

330      $\delta^{15}N$ (NO_3^-) values indicate biogenic soil emissions and fossil-combustion, respectively. (Elliott et al.,

331   2019)

332   Along with nitrogen isotope, heavier oxygen isotopes were also enriched in NO_3^- during the winter

333   compared to the summer, when the weight-mean of $\delta^{17}O$, $\delta^{18}O$, and $\Delta^{17}O$ in NO_3^- were 70.4‰ ± 5.4 ‰,

334   82.0‰ ± 6.2 ‰, and 27.7‰ ± 2.2 ‰ for the winter and 57.3‰ ± 4.9 ‰, 65.7‰ ± 6.2 ‰, and 23.2‰ ±

335   2.2 ‰ for the summer. These results of high winter and low summer $\Delta^{17}O$ (NO_3^-) were consistent with

336   previous observations at urban Beijing (He et al., 2018; Wang et al., 2019b; Figure 2b), indicative of

337   relatively greater contribution of nighttime oxidation pathways in winter. It is also noteworthy that our

338   summer and winter $\Delta^{17}O$ (NO_3^-) values were similar to annual $\Delta^{17}O$ (NO_3^-) values of an urban (Sapporo)

339   and a rural (Rishiri) site in Japan, respectively (Nelson et al., 2018). It is likely suggestive that the winter

340      $\Delta^{17}O$ value in Seoul has undergone a considerable atmospheric processing on a regional scale.

341   Given that $PM_{2.5}$ concentrations reflect the seasonality, atmospheric chemical composition and

342   meteorological properties were examined in relation to $PM_{2.5}$ concentrations (Figure 3). Clearly, for the

343   winter samples with $PM_{2.5}$ concentration greater than 40 μg m^{-3}, meteorological conditions varied

344   relative to low PM$_{2.5}$ samples; relatively high temperature and RH staying at 0 °C to 10 °C and 45 % to

345   65 %, respectively, and low wind speed of 1 m s^{-1} to 2 m s^{-1}, representing the meteorological

346   characteristics of winter PM$_{2.5}$ episodes. Particularly in winter, a strong linearity of PM$_{2.5}$ was found

347   with most chemical constituents considered in this study, such as SIA species, TN, NOR, and SOR.

348   However, although being elevated in levels, NO$_2$ and O$_3$ mixing ratios showed non-linearity with PM$_{2.5}$

349   concentrations. Isotope ratios were correlated either linearly or inversely with PM$_{2.5}$ concentrations. In

350   winter, Δ^{17}O (NO$_3^-$) showed the best correlation with PM$_{2.5}$ concentrations but δ^{15}N (NO$_3^-$) was

351   inversely related with PM$_{2.5}$ level.

352

3.2. Graphical representation of dual isotopes: Δ^{17}O and δ^{15}N of NO$_3^-$

354   The isotope ratios of source endmembers are scarce in the study region and in the aerosol measurements

355   and the isotope fractionation effect during gas-to-particle conversion is often estimated with

356   thermodynamic constants and reasonable assumptions. In this regard, the graphical representation of

357   dual isotopes enables the complex signatures of atmospheric samples to be distinguished and allows

358   their oxidation processes to be constrained. Figure 4 displayed measured δ^{15}N (NO$_3^-$) and Δ^{17}O (NO$_3^-$)

359   coordinates with related chemical parameters in colors.

360   In Figure 4a and b, the range of Δ^{17}O (NO$_3^-$) endmembers for the three NO$_3^-$ oxidation pathways

361   calculated in Sect. 2.3.2. were presented by black dotted boxes, of which domains of the three pathways

362   are successfully distinguished. The Δ^{17}O (NO$_3^-$) of all samples fell into the predicted ranges of the Δ^{17}O

363   endmembers, but were separated into seasonal groups. Most of summer Δ^{17}O (NO$_3^-$) values indicate

364   NO$_3^-$ (R4) pathway. It is in accordance with what has been reported in temperate areas during summer

365   (Alexander et al., 2009; Michalski et al., 2003). In field measurements of δ^{15}N (NO$_3^-$) and δ^{18}O (NO$_3^-$)

366   in Chinese cities, the proportional contribution of OH-oxidation pathway was significantly correlated

367   with latitudes (Zong et al., 2020), confirming the evidence of the NO$_3^-$ formation through OH oxidation

368   depending on UV radiation intensity.

369   In comparison, more than half of winter samples are located in the domain indicating NO$_3^-$ (R7) and

370   (R8) pathways. Particularly, for winter samples with NO$_3^-$ mass concentration higher than ~ 30 μg m^{-3},

371   Δ^{17}O (NO$_3^-$) values clearly represent the (R7) pathway. The winter Δ^{17}O (NO$_3^-$) was proportional to

372   nitrogen oxidation ratio (NOR, Figure 4c), indicative of efficient conversion of NO$_x$ to NO$_3^-$ via O$_3$

373   oxidation pathways. In the summer periods when NO$_3^-$ concentrations were relatively high (above ~ 3

374   μg m^{-3}), the contributions of O$_3$ oxidation pathways became elevated, which is a similar pattern to what

375 was observed in the winter. This result suggests that the O_3 oxidation pathways are likely to be
376 responsible for the rapid conversion of particulate NO_3^- observed during winter and summer $PM_{2.5}$
377 episodes in the study region.

378 The formation of N_2O_5 (R6) is dependent on both NO_2 and O_3, which are reciprocally correlated in
379 source regions. The equilibrium of R6 shifts to N_2O_5 at low temperature and its lifetime against
380 photolysis is long under the low sunlight. For these reasons, the dark formation of NO_3^- (R7) would be
381 favorable in urban outflows in winter. The hydrolysis of N_2O_5 on aerosol surface (R7) is highly
382 dependent on RH, aerosol liquid water content (AWLC), and chemical composition (Hallquist et al.,
383 2003; Wahner et al., 1998). To evaluate the $\Delta^{17}O$ (NO_3^-) signature observed, we calculated ALWC and
384 acidity of aerosol, pH using ISORROPIA II model (Sect. 2.4.). Given the high concentration of nano-
385 particles from various sources in the urban areas, it is assured that aerosol surface is enough for NO_3^-
386 (R7) pathway. The calculated ALWC was higher by 90 % (19.1 ± 22.8 μg m^{-3}) in the winter and lower
387 by 21 % (7.8 ± 5.2 μg m^{-3}) in the summer relative to the annual mean of the two years. When NO_3^- mass
388 concentrations were greater than ~ 3 μg m^{-3} in the summer and ~ 30 μg m^{-3} in the winter, ALWC was
389 14.3 μg m^{-3} and 31.7 μg m^{-3}, respectively, which were greater by 166 % and 183 % than the seasonal
390 mean, respectively (Figure 4d). Furthermore, the high $\Delta^{17}O$ (NO_3^-) and ALWC coincided with lower
391 bound (about 4) of winter pH varying from 4 to 6, whereas aerosol pH was 2-3 during the summer. The
392 low aerosol pH concurrent with the high $\Delta^{17}O$ (NO_3^-) and ALWC is coherent with the aqueous-phase
393 HNO_3 formation on liquid aerosol through R7.

394 While $\Delta^{17}O$ (NO_3^-) allows insights into the oxidation pathway of NO_3^-, $\delta^{15}N$ (NO_3^-) values are affected
395 by various factors, most of which are not well constrained due to the complicated chemistry and key
396 roles of nitrogen oxides in the Earth's environment. In this study, $\delta^{15}N$ (NO_3^-) variability versus $PM_{2.5}$
397 concentration resembled the variability of NO_2 versus $PM_{2.5}$ concentration (Figure 3f and o), implying
398 a close link between NO_2 oxidation and $\delta^{15}N$ (NO_3^-). Therefore, in addition to the role of $\Delta^{17}O$ (NO_3^-)
399 as a tracer of NO_3^- oxidation pathway, we evaluated whether a variation of $\delta^{15}N$ (NO_3^-) indicates NO_x
400 oxidation efficiency between NO and NO_2 (Freyer et al., 1993; Nelson et al., 2018; Walters et al., 2016).
401 A possible effect on $\delta^{15}N$ during NO_x photochemical cycling cannot be predicted in the same way under
402 varying conditions, e.g., depending on abundances of NO, NO_2, and O_3. The shift in $\delta^{15}N$ (NO_2) relative
403 to $\delta^{15}N$ (NO_x) in the atmosphere will change depending on f_{NO2} and temperature-dependent $\alpha_{NO2/NO}$
404 (Freyer et al., 1993; Li et al., 2020; Walters et al., 2016). When O_3 mixing ratio is high, NO is almost
405 completely oxidized to NO_2, leading to an increasing f_{NO2} value, and the $\delta^{15}N$ (NO_2) should correspond
406 to the $\delta^{15}N$ of NO_x sources (Freyer et al., 1993).

In the dual isotope coordinates of $\delta^{15}N$ (NO_3^-) and $\Delta^{17}O$ (NO_3^-) (Figure 4), it is evident the samples taken during a record-breaking winter $PM_{2.5}$ pollution events are associated with the lower bound values of $\delta^{15}N$ (NO_3^-) (-1 to 4 ‰) and the highest $\Delta^{17}O$ (NO_3^-) values (28 to 31 ‰). Simultaneous measurements of PM_1 chemical composition in Seoul and Beijing demonstrated that the regionally-processed air masses were long-range transported to Seoul within approximately 2 days during these episodes (Kim et al., 2020a). Their NO_2/O_3 ratio (1 to 2) was clearly lower with higher f_{NO2} (0.7 to 0.8) compared to the other winter samples (Figure 4g and h). This result implies that O_3 level was high enough to efficiently oxidize NO to NO_2 during the severe $PM_{2.5}$ pollution events. In this condition, the shift in $\delta^{15}N$ (NO_2) relative to $\delta^{15}N$ (NO_x) is insignificant and consequently, $\delta^{15}N$ (NO_2) would be lower than those of other winter samples unless both emission sources and $\alpha_{NO2/NO}$ changed significantly. Considering that NO_3^- is the key driver of the high $PM_{2.5}$ in Seoul, the higher degree of NO_x oxidation efficiency is worth highlighting, in conjunction with a strong linear relationship between $\Delta^{17}O$ (NO_3^-) and NOR (Figure 4c) revealing an efficient conversion of NO_2 to NO_3^- through NO_3^- pathway (R5+R6+R7+R8) via O_3. The seasonally bifurcated $\delta^{15}N$ (NO_3^-) can be attributed primarily to the NO_x sources, which will be discussed in Section 3.4.

3.3. Contributions of major HNO_3 oxidation pathways

Combining the $\Delta^{17}O$ (NO_3^-) measurements and the calculation of $\Delta^{17}O$ transferred from O_3 to HNO_3, the contributions of three major NO_3^- formation pathways were quantitatively accounted, despite the inherent uncertainties in the calculation (Sect. 2.5.).

NO_3^- pathway (R4) dominated the total NO_3^- formation (87 ± 6 %) in summer. In contrast, the nighttime pathways through N_2O_5 and NO_3 (pathways R7 and R8) were responsible for 24 % and 14 % of the NO_3^- formation in the winter, respectively. The contribution increased further to 40 % and 30 %, respectively, on haze days when $PM_{2.5}$ concentration exceeded 75 μg m^{-3}, national air quality standard for "very bad" alert. The significant nighttime oxidation of NO_3^- has been observed broadly at urban sites in Northeast Asia. The results of this study are consistent with those conducted in Beijing, showing low $\Delta^{17}O$ values in summertime (about 17 ‰ to 25 ‰) and substantially high $\Delta^{17}O$ values (about 25 ‰ to 34 ‰) in wintertime when NO_3^--driven $PM_{2.5}$ haze pollution occurred (He et al., 2018; Song et al., 2020; Wang et al., 2019b). In general, nighttime pathways accounted for more than 60 % and up to 97 % in Beijing (He et al., 2018; Song et al., 2020; Wang et al., 2019b). From a global perspective, the chemical transport model demonstrated that N_2O_5 heterogeneous hydrolysis was comparably important

438   as $NO_2 + OH$ (41 %) for NO_3^- formation at below 1km altitude (Alexander et al., 2020).

439   It is noteworthy that although the seasonal patterns are similar in Northeast Asia, the average

440   proportional contributions estimated from $\Delta^{17}O$ (NO_3^-) are highly sensitive to input parameters (i.e, f_{O3}

441   and $\Delta^{17}O\text{-}O_3^*$). In this study, the seasonal f_{O3} was assumed to be equal to those estimated for Beijing

442   and set to 0.858 ± 0.05 and 0.918 ± 0.05 for the warm and cold months, respectively (Wang et al.,

443   2019b), which are comparable to other estimates for Beijing (0.86) and Shanghai (0.97) (He et al., 2018,

444   2020) and the annual-mean of 0.85 in a global model (Alexander et al., 2020).

445   The uncertainty associated with $\Delta^{17}O\text{-}O_3^*$ has been recognized as the largest source of uncertainty in

446   estimating NO_3^- production pathways from $\Delta^{17}O$ (NO_3^-) (Alexander et al., 2009, 2020). In this study,

447   the $\Delta^{17}O\text{-}O_3^*$ of 37.5 ± 2.2 ‰ was averaged from previous observations, corresponding to $\Delta^{17}O$-bulk

448   O_3 of 25 ‰ (Ishino et al., 2017; Vicars et al., 2012; Vicars and Savarino, 2014). Our mean $\Delta^{17}O\text{-}O_3^*$ of

449   37.5 ‰ was 2.8 ‰ higher and 1.5 ‰ lower than what was used in the field studies (Song et al., 2020;

450   Wang et al., 2019b) and the studies (He et al., 2018, 2020), respectively, for urban Beijing and Shanghai.

451   When sensitivity test was conducted for the proportional contribution of the three oxidation pathways,

452   a 2.8 ‰ change in $\Delta^{17}O\text{-}O_3^*$ value caused 1.6 ‰, 2.1 ‰, and 2.5 ‰ change in the endmember for (R4),

453   (R7), and (R8) pathway, respectively. As a result, the average contribution of the nighttime pathways,

454   including NO_3^- (R7) and NO_3^- (R8), increased to 23 % in summer and 65 % in winter. This suggests

455   that a proper use of key parameters driving endmember values is pre-requisite for more realistic

456   quantification of NO_3^- oxidation pathway contributions.

457

3.4. Major NO_x emission sources

459   To investigate major emission sources of atmospheric NO_x in Seoul, $\delta^{15}N$ (NO_x) in the atmosphere

460   ($\delta^{15}N$ (NO_x)$_{atmosphere}$) was estimated from measured $\delta^{15}N$ (NO_3^-) considering nitrogen isotopic

461   fractionation effects (ε_N) based on a dual isotopes approach ($\Delta^{17}O$ and $\delta^{15}N$). Estimated ε_N values were

462   5.9 ± 1.5 ‰ and of 12.2 ± 0.5 ‰ and accordingly, the $\delta^{15}N$ (NO_x)$_{atmosphere}$ was -8.7 ± 3.3 ‰ and $-5.8 \pm$

463   4.2 ‰ in summer and winter, respectively. The larger winter ε_N reveals the enhanced contribution of

464   nighttime oxidation pathway via N_2O_5. As a result, a seasonal difference in $\delta^{15}N$ (NO_x)$_{atmosphere}$ was as

465   small as 2.9 ‰ on average, which is suggestive of little seasonal difference in major NO_x emission

466   source in Seoul.

467   Figure 5 displays the measured $\delta^{15}N$ (NO_3^-) and estimated $\delta^{15}N$ (NO_x)$_{atmosphere}$ of individual samples

468   together with $\delta^{15}N$ (NO$_x$) domains of emission source endmembers reported in literature; biogenic soil

469   (driven by fertilizer use; -35.1 ± 10.2 ‰) (Felix and Elliott, 2014; Li and Wang, 2008; Yu and Elliott,

470   2017), biomass burning (1.8 ± 1.8 ‰) (Fibiger and Hastings, 2016), vehicle emissions (-2.5 ± 1.5 ‰)

471   (Walters et al., 2015), and coal combustion (14.2 ± 4.5 ‰) (Felix et al., 2012; Heaton, 1990). Both in

472   summer and winter, $\delta^{15}N$ (NO$_x$)$_{atmosphere}$ are the closest to the domain of vehicle emissions $\delta^{15}N$ (NO$_x$),

473   highlighting the largest contribution of vehicle emissions to NO$_x$ in Seoul (Figure 5). However, the

474   winter $\delta^{15}N$ (NO$_3^-$) without isotope fractionation effect apparently point to coal emissions, which could

475   lead to misleading conclusions about major NO$_x$ sources. This result is supported by a better correlation

476   of NO$_2$ with CO than with SO$_2$ for both seasons. According to a (anthropogenic) bottom-up emissions

477   inventory, the Clean Air Policy Support System (CAPSS), total mobile sources account for about two-

478   third of NO$_x$ emissions in Korea, followed by combustion sources such as energy and manufacturing

479   industries (33 %). The highest NO$_2$ column densities are distinct in Seoul Metropolitan Areas (SMA),

480   which is mostly due to the emissions from transportation (Kim et al., 2020b). Our results of the isotope

481   measurements are in fairly good agreement with the national emission inventories and satellite

482   observations, highlighting the largest contribution of vehicle emissions to NO$_x$ sources in Seoul.

483   Other than vehicle emissions, the lower bound summer $\delta^{15}N$ (NO$_x$)$_{atmosphere}$ and the upper bound winter

484     $\delta^{15}N$ (NO$_x$)$_{atmosphere}$ were relatively closer to the $\delta^{15}N$ (NO$_x$) of fertilized soil emissions and coal-

485   combustion, respectively. These seasonally distinct contributions from soil emissions and coal

486   combustion were consistent with the results from previous studies conducted in China, revealing

487   common seasonal emission characteristics on a regional scale in East Asia. It was evident that the upper

488   bound winter $\delta^{15}N$ (NO$_2$)$_{atmosphere}$ coincided with elevated SO$_4^{2-}$/ NO$_3^-$ mass ratio by 2-3 times. During

489   these periods, trajectory analysis indicates that air masses originated from cold regions in northeastern

490   China, such as Liaoning province, where heavy and coal-fired industries are located. In Beijing located

491   in northeastern China, coal combustion is an important fossil-fuel source as the highest contribution

492   source to atmospheric NO$_x$ emissions during winter, about 30 to 40 %, regardless of approaches used

493   for estimating NO$_3^-$ oxidation pathways, either $\Delta^{17}O$ or $\delta^{18}O$ (Li et al., 2019; Song et al., 2019, 2020;

494   Zong et al., 2020). Thus, in this study, the upper bound winter $\delta^{15}N$ (NO$_x$)$_{atmosphere}$ suggests enhanced

495   contributions of coal combustion to atmospheric NO$_x$ emissions. It is particularly noteworthy that the

496   lower winter $\delta^{15}N$ (NO$_3^-$) and thus relatively lower contribution of coal combustion confirms the recent

497   trend that emissions from coal combustion have been reduced in China (Cheng et al., 2019; Tong et al.,

498   2018). Our study was conducted in later years (2018-2019) than their studies (2013-2017), of which

499     $\delta^{15}N$ (NO$_3^-$) values were rather comparable to the winter mean $\delta^{15}N$ (NO$_3^-$) observed in Seoul during

500   January 2014 ~ February 2016 (11.9 ± 2.5 ‰; Park et al., 2018). The lower bound of winter $\delta^{15}N$ (NO$_3^-$)

501 values associated with the highest NO_3^- and $PM_{2.5}$ concentrations (Figures 3 and 4) was considered a

502 result of complex effects of isotopic fractionation, as discussed above.

503 This study region is under influence of various biomass burning sources throughout a year, such as

504 agricultural combustion in vicinities of Seoul and over eastern China from spring to fall (Chen et al.,

505 2017; Zhao et al., 2017), wild fires over Siberia and Russian Far East in summer (van der Werf et al.,

506 2010), and residential biomass combustion for heating over east Asia in winter. Some winter $\delta^{15}N$

507 $(NO_x)_{atmosphere}$ values fell in the $\delta^{15}N$ (NO_x) range of biomass burning endmember (Fibiger and Hastings,

508 2016; Figure 5). When assessing contributions of biomass burning based on $\delta^{15}N$ $(NO_x)_{atmosphere}$ and few

509 endmember $\delta^{15}N$ (NO_x), however, caution should be exerted considering the fact that $\delta^{15}N$ (NO_x) varied

510 among biomass types from -7 to 12‰ (Fibiger and Hastings, 2016) and there is currently a lack of

511 understanding of biomass combustion that could potentially affect air quality in Seoul.

512

4. Conclusions and outlook

514 5. Our $\delta^{15}N$ and $\Delta^{17}O$-based study confirms that vehicle emissions are the main source of NO_3^- in $PM_{2.5}$ in

515 Seoul during the summer and the winter. In addition, the qualitative estimates of NO_x emission sources

516 provide suggestive evidence for enhanced contributions from coal combustion and biogenic soil

517 emissions in the winter and the summer, respectively. Moreover, severe winter haze events with daily

518 $PM_{2.5}$ exceeding 100 μg m^{-3} were mainly driven by NO_3^- (up to ~60 % in $PM_{2.5}$). Reducing NO_x

519 emissions from vehicles is, therefore, essential for an effective mitigation measure to improve fine

520 aerosol pollution in the study region. Particularly, the highest $PM_{2.5}$ was concurrent with the highest

521 NOR and $\Delta^{17}O$ (NO_3^-), and the lowest $\delta^{15}N$ (NO_3^-), revealing the heterogeneous conversion of HNO_3 to

522 particulate NO_3^- through O_3 oxidation pathway during the winter haze episodes. The multiple-isotope

523 signatures of particulate NO_3^-, including ^{17}O, ^{18}O, and ^{15}N, highlight the secondary nature of fine aerosol

524 pollution intimately coupled with the photochemical oxidation process.

525 While our results demonstrate that $\delta^{15}N$ and $\Delta^{17}O$ are robust tracers for major NO_x sources, quantitative

526 source apportionment using the isotope method requires further elaboration of isotope

527 equilibrium/kinetic fractionation effects involved in photochemical cycling of nitrogen oxides and $\delta^{15}N$

528 of NO_x source endmembers representing local or regional emissions in East Asia. In well-designed field

529 studies, the $\delta^{15}N$ and $\Delta^{17}O$ measurements of multiphase and their vertical structures allow us to test the

530 isotope fractionation effects suggested by laboratory experiments and theoretical calculations, and to

531 characterize the atmospheric processing that influence them. In addition, there is an urgent need to

532 document the $\delta^{15}N$ (NO_x) values of emissions from vehicles with/without selective catalytic reduction

533 (SCR) and from biomass combustion as a function of biomass type and combustion conditions.

534 Consequently, a comprehensive and quantitative understanding of the oxidation pathways and emission

535 sources of nitrogen oxides using $\delta^{15}N$ and $\Delta^{17}O$ measurements will be able to elucidate detailed

536 mechanisms driving severe haze development in megacities of northeast Asia, including Seoul.

537

538 **Acknowledgement**

539 This research was supported by the National Strategic Project-Fine Particle of the National Research

540 Foundation of Korea (NRF), funded by the Ministry of Science and ICT (MSIT), Ministry of

541 Environment (ME), and Ministry of Health and Welfare (MOHW) (2017M3D8A1092015). Funding to

542 S. Lim was provided by the National Research Foundation of Korea (NRF) from the Ministry of Science

543 and ICT (2018R1D1A1B07050849). M. Lee thanks for the support from NRF (2020R1A2C3014592).

544 J. Savarino thanks the French National Research Agency (Investissements d'avenir grant ANR-15-

545 IDEX-02) and the INSU programme LEFE-CHAT for supporting the stable isotope laboratory. This is

546 publication 4 of PANDA platform on which isotope analyses were performed.

547

548 **Table and figures**

549 **Tables**

550

551 **Table 1. Measurement summary of PM$_{2.5}$ chemical constituents and isotopic composition in Seoul**
552 **during the sampling period of May. 2018-Mar. 2019. Arithmetic mean ± 1 standard**
553 **deviation (mass fraction, %) for mass concentrations and concentration-weight mean ± 1**
554 **standard deviation for isotope ratios.**

555

Constituents	Summer (n = 13)	Winter (n = 18)
PM$_{2.5}$ (µg m^{-3})	22.7 ± 6.9	61.7 ± 39.2
TC	4. 6 ± 1.4 (20 %)	15.2 ± 4.5 (25 %)
TN	1.9 ± 1.0 (8 %)	11.8 ± 7.7 (19 %)
NO$_3^-$	0.8 ± 0.9 (4 %)	29.7 ± 22.1 (48 %)
NH$_4^+$	1.9 ± 0.8 (8 %)	11.7 ± 8.4 (19 %)
SO$_4^{2-}$	5.3 ± 2.1 (23 %)	11.5 ± 9.2 (19 %)
[NH$_4^+$]/([SO$_4^{2-}$]+[NO$_3^-$]) equiv. ratio	0.83 ± 0.08	0.94 ± 0.09
$\delta^{15}N$ (NO$_3^-$)	-0.7 ± 3.3	3.8 ± 3.7
$\delta^{17}O$	57.3 ± 4.9	70.4 ± 5.4
$\delta^{18}O$	65.7 ± 6.2	82.0 ± 6.2
$\Delta^{17}O$	23.2 ± 2.2	27.7 ± 2.2

556
557

Figures.

Figure 1. Location of the study region. (a) Seoul metropolitan area in South Korea and (b) sampling site of Korea University campus in the northeast Seoul.

Figure 2. (a) $\delta^{15}N$ (NO$_3^-$) and (b) $\Delta^{17}O$ (NO$_3^-$) PM$_{2.5}$ observed in Northeast Asia are compared: Seoul in this study (red), Beijing (brown), Shanghai (orange), and Guangzhou (light) in China, and Rishiri (green) and Sapporo (blue) in Japan during summer (circle) and winter (square). Marker indicates mean value (concentration-weighted average for Seoul samples in this study), and lower and upper whiskers denote minimum and maximum values (This study; He et al., 2018; Lim et al., 2020; Nelson et al., 2018), mean ± standard deviation (Song et al., 2019; Wang et al., 2019b), or 25th and 75th percentiles (Zong et al., 2020).

Figure 3. Relationships of PM$_{2.5}$ mass concentration with meteorological parameters (a-c), concentrations of reactive gases (d-f, k) and aerosol chemical constituents (g-j, l-n), and N and O isotopic compositions (o-q) measured in Seoul during the summer (open circle) and the winter (blue ribbon).

Figure 4. The relationship of measured $\delta^{15}N$ (NO$_3^-$) and $\Delta^{17}O$ (NO$_3^-$) values with key parameters during the summer (open circle) and winter (closed ribbon). The predicted $\Delta^{17}O$ (NO$_3^-$) values are presented as dotted rectangles for the tree major NO$_3^-$ formation pathways (R4, R7, and R8, see Sect. 2.3.2 for details) in (a) summer and (b) winter. Data are color coded by (a) and (b) nitrate concentrations, (c) NOR, (d) ALWC, (e) pH, (f) [NH$_4^+$]/([SO$_4^{2-}$]+[NO$_3^-$]) equivalent ratio, (g) NO$_2$/O$_3$ ratio, and (h) f$_{NO2}$. Marker size is proportional to PM$_{2.5}$ concentration ranging from 10 μg m^{-3} to 100 μg m^{-3}.

Figure 5. Variations in measured $\delta^{15}N$ (NO$_3^-$) (open) and estimated $\delta^{15}N$ (NO$_x$)$_{atmosphere}$ (closed) in Seoul during the summer (circle) and winter (triangle). The $\delta^{15}N$ (NO$_x$) range (mean ± 1sd) of source end members are distinguished by dotted boxes in different colors: coal combustion (14.2 ± 4.5 ‰) (Felix et al., 2012; Heaton, 1990), biomass burning (1.8 ±1.8 ‰) (Fibiger and Hastings, 2016), vehicle emissions (-2.5 ± 1.5 ‰) (Walters et al., 2015), and biogenic soil emissions (-35.1 ± 10.2 ‰) (Felix and Elliott, 2014; Li and Wang, 2008; Yu and Elliott, 2017).

587

Figure 1. Location of the study region. (a) Seoul metropolitan area in South Korea and (b) sampling site of Korea University campus in the northeast Seoul.

590

b)
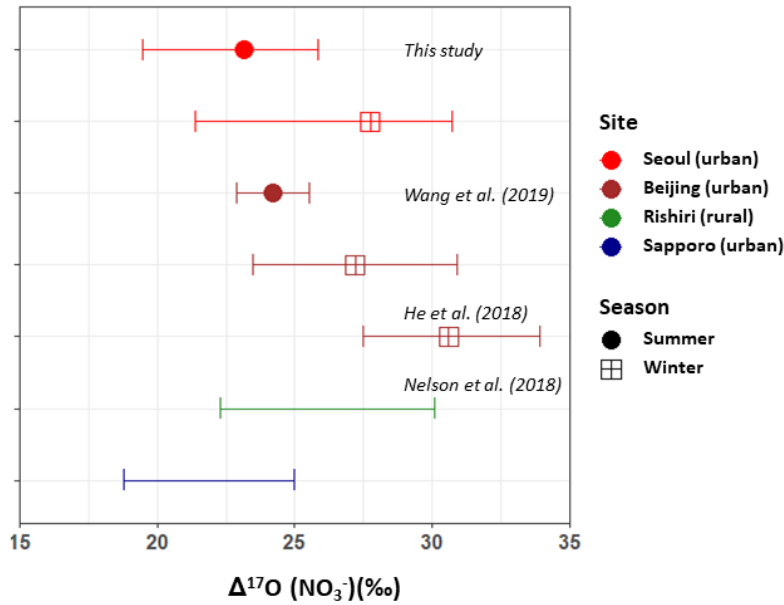
591

592 **Figure 2. (a) $\delta^{15}N$ (NO$_3^-$) and (b) $\Delta^{17}O$ (NO$_3^-$) PM$_{2.5}$ observed in Northeast Asia are compared:**
593   **Seoul in this study (red), Beijing (brown), Shanghai (orange), and Guangzhou (light) in**
594   **China, and Rishiri (green) and Sapporo (blue) in Japan during summer (circle) and**
595   **winter (square). Marker indicates mean value (concentration-weighted average for**
596   **Seoul samples in this study), and lower and upper whiskers denote minimum and**
597   **maximum values (This study; He et al., 2018; Lim et al., 2020; Nelson et al., 2018), mean**
598   **± standard deviation (Song et al., 2019; Wang et al., 2019b), or 25th and 75th percentiles**
599   **(Zong et al., 2020).**

600

601
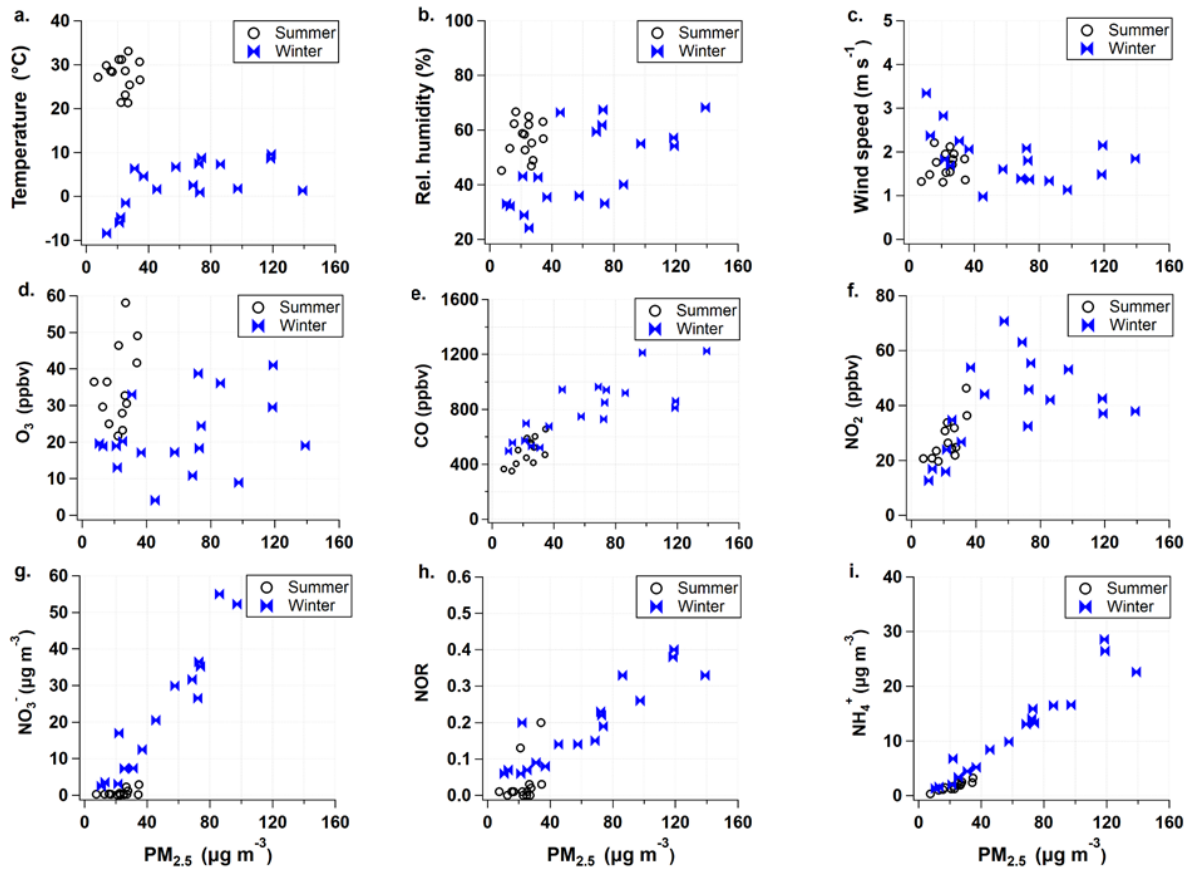
602
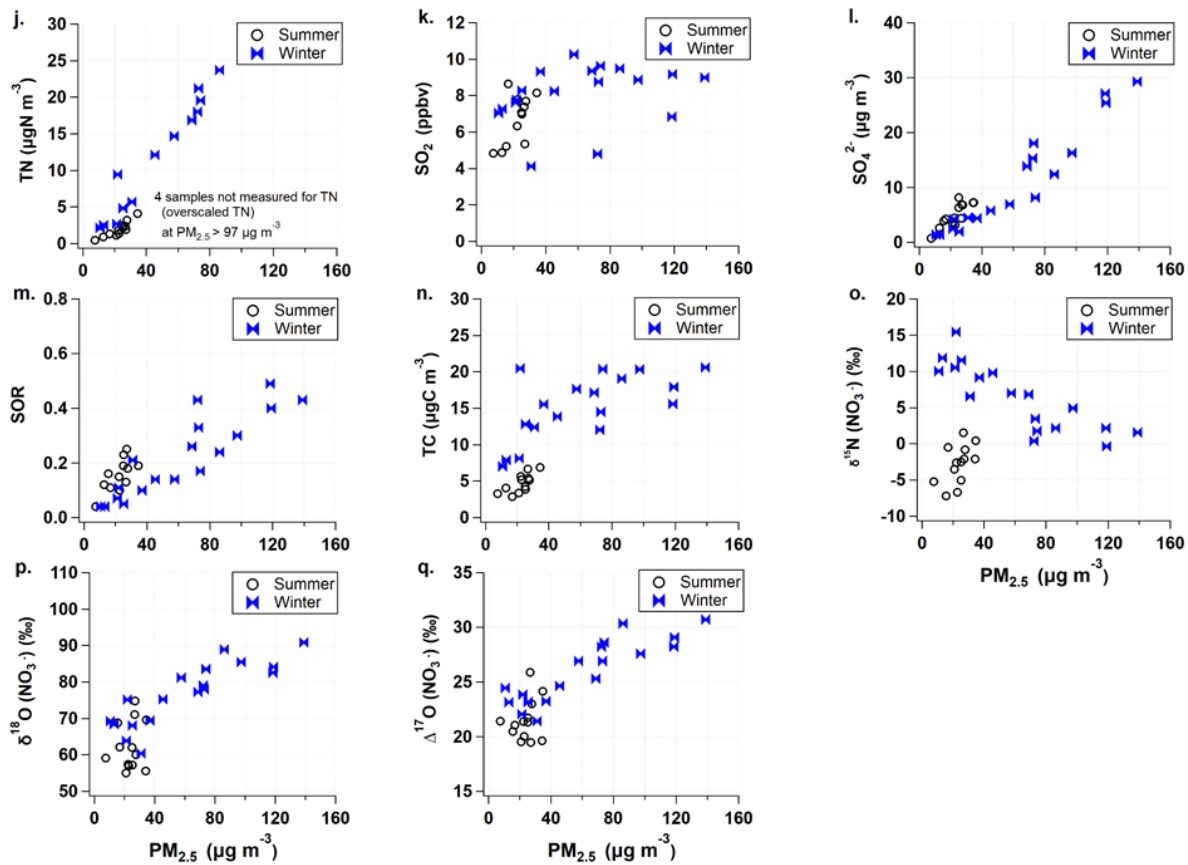
603

Figure 3. Relationships of PM$_{2.5}$ mass concentration with meteorological parameters (a-c),
604

concentrations of reactive gases (d-f, k) and aerosol chemical constituents (g-j, l-n),
605

and N and O isotopic compositions (o-q) measured in Seoul during the summer (open
606

circle) and the winter (blue ribbon).
607

608

609
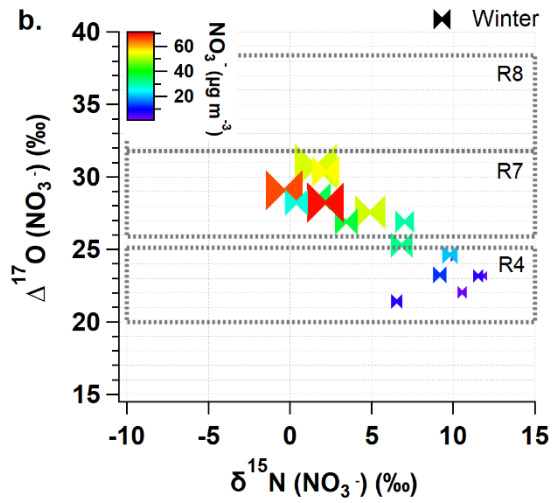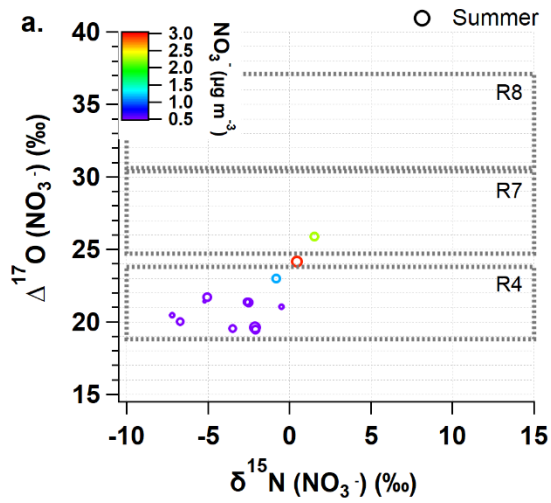
610
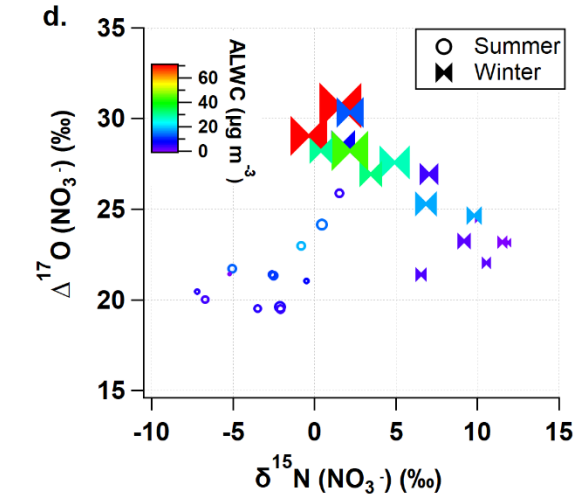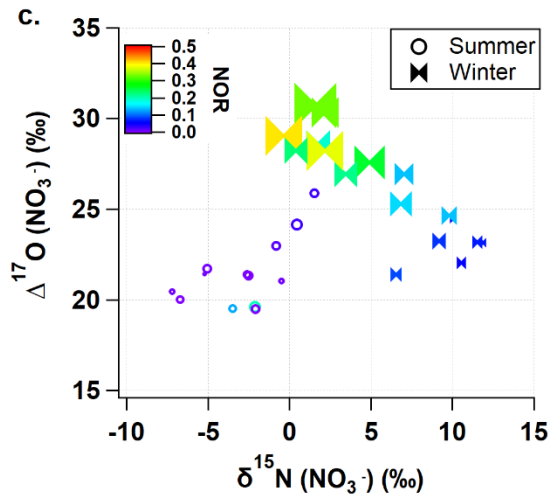
611
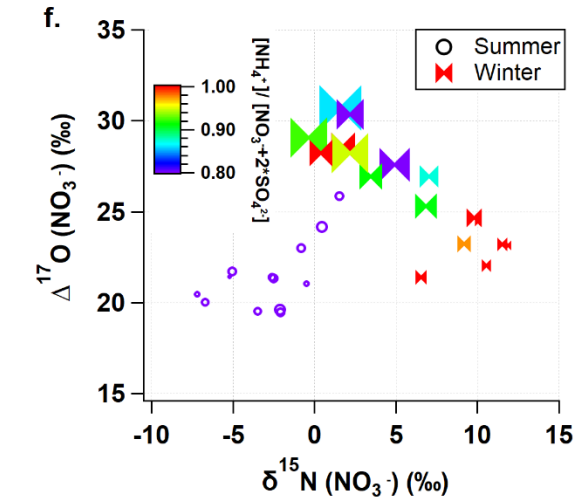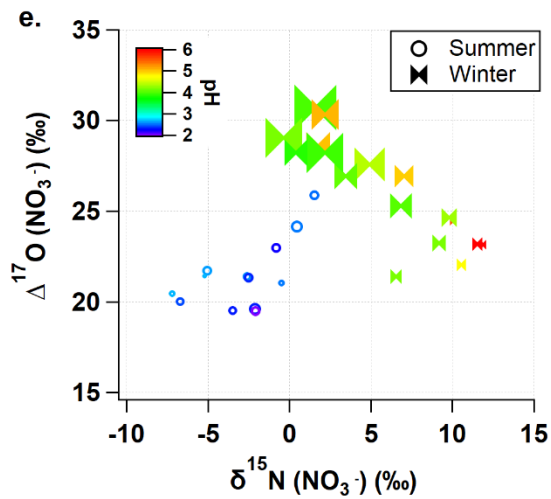
612
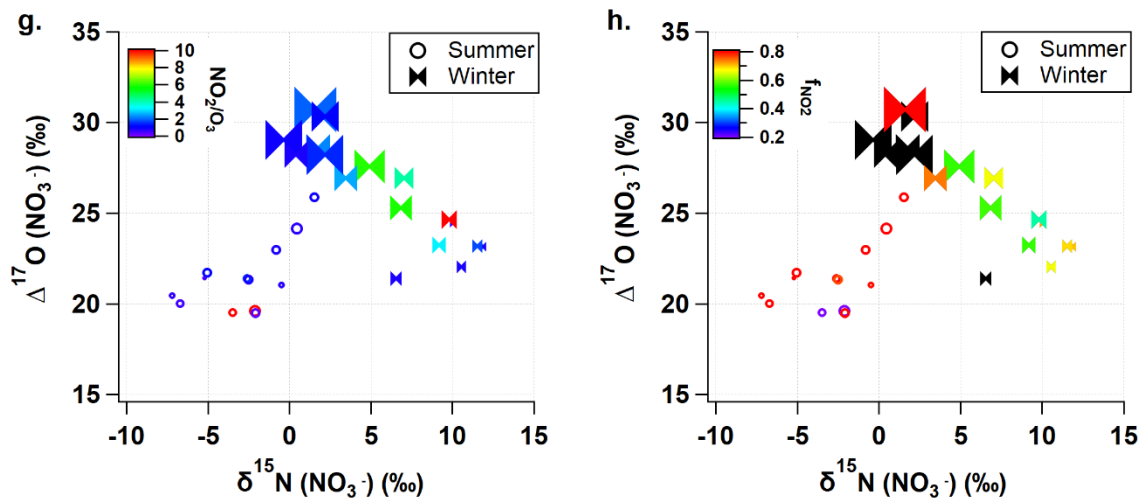
613

614   **Figure 4. The relationship of measured $\delta^{15}N$ (NO$_3^-$) and $\Delta^{17}O$ (NO$_3^-$) values with key parameters**

615   **during the summer (open circle) and winter (closed ribbon). The predicted $\Delta^{17}O$ (NO$_3^-$)**

616   **values are presented as dotted rectangles for the tree major NO$_3^-$ formation pathways**

617   **(R4, R7, and R8, see Sect. 2.3.2 for details) in (a) summer and (b) winter. Data are color**

618   **coded by (a) and (b) nitrate concentrations, (c) NOR, (d) ALWC, (e) pH, (f)**

619   **[NH$_4^+$]/([SO$_4^{2-}$]+[NO$_3^-$]) equivalent ratio, (g) NO$_2$/O$_3$ ratio, and (h) f_{NO2}. Marker size is**

620   **proportional to PM$_{2.5}$ concentration ranging from 10 µg m^{-3} to 100 µg m^{-3}.**

621
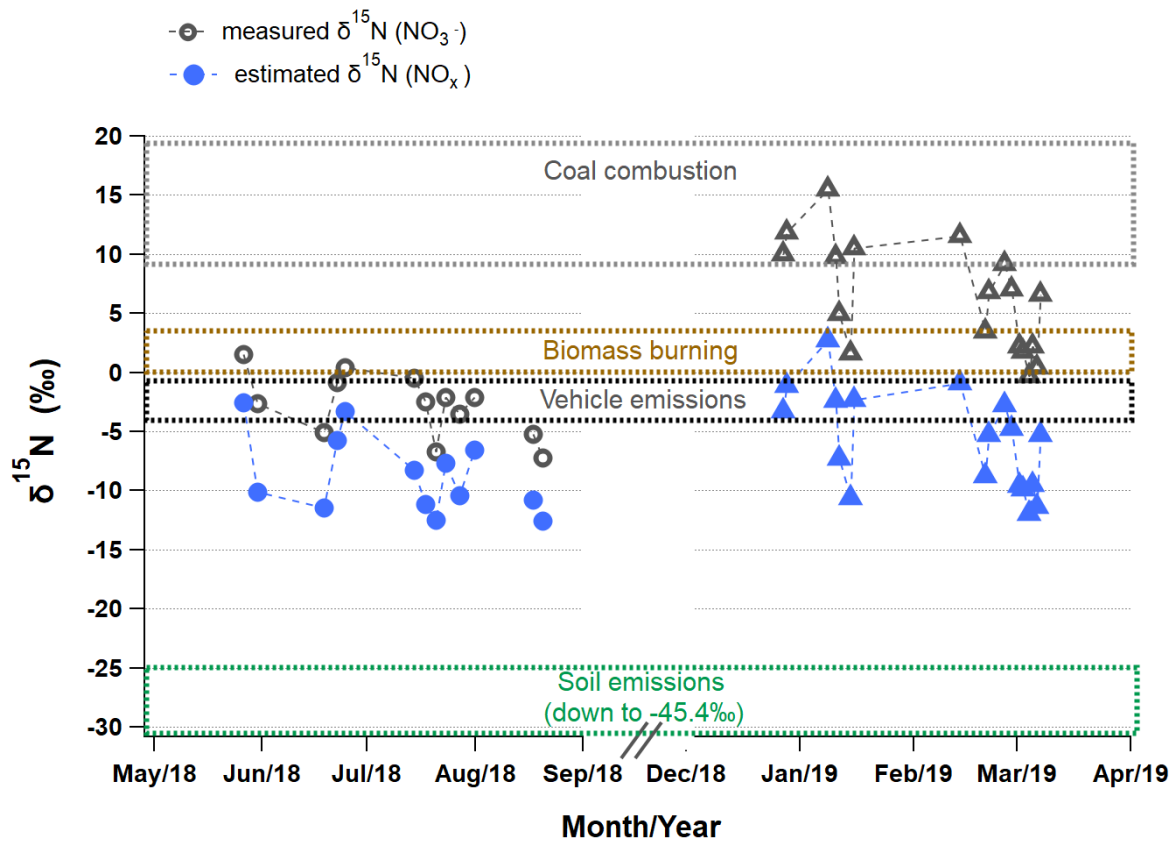
622

623 **Figure 5. Variations in measured $\delta^{15}N$ (NO$_3^-$) (open) and estimated $\delta^{15}N$ (NO$_x$)$_{atmosphere}$ (closed) in**

624   **Seoul during the summer (circle) and winter (triangle). The $\delta^{15}N$ (NO$_x$) range (mean ±**

625   **1sd) of source end members are distinguished by dotted boxes in different colors: coal**

626   **combustion (14.2 ± 4.5 ‰) (Felix et al., 2012; Heaton, 1990), biomass burning (1.8 ±1.8**

627   **‰) (Fibiger and Hastings, 2016), vehicle emissions (-2.5 ± 1.5 ‰) (Walters et al., 2015),**

628   **and biogenic soil emissions (-35.1 ± 10.2 ‰) (Felix and Elliott, 2014; Li and Wang, 2008;**

629   **Yu and Elliott, 2017).**

630

631

632   **References**

633   Alexander, B., Hastings, M. G., Allman, D. J., Dachs, J., Thornton, J. A. and Kunasek, S. A.:

634   Quantifying atmospheric nitrate formation pathways based on a global model of the oxygen isotopic

635   composition (Δ^{17}O) of atmospheric nitrate, Atmos. Chem. Phys., 9(14), 5043–5056,

636   doi:10.5194/acp-9-5043-2009, 2009.

637   Alexander, B., Sherwen, T., Holmes, C. D., Fisher, J. A., Chen, Q., Evans, M. J. and Kasibhatla, P.:

638   Global inorganic nitrate production mechanisms: comparison of a global model with nitrate isotope

639   observations, Atmos. Chem. Phys., 20(6), 3859–3877, doi:10.5194/acp-20-3859-2020, 2020.

640   Carslaw, D. C. and Ropkins, K.: openair — An R package for air quality data analysis, Environ.

641   Model. Softw., 27–28, 52–61, doi:10.1016/j.envsoft.2011.09.008, 2012.

642   Casciotti, K. L., Sigman, D. M., Hastings, M. G., Böhlke, J. K. and Hilkert, A.: Measurement of the

643   oxygen isotopic composition of nitrate in seawater and freshwater using the denitrifier method, Anal.

644   Chem., 74(19), 4905–4912, doi:10.1021/ac020113w, 2002.

645   Chen, J., Li, C., Ristovski, Z., Milic, A., Gu, Y., Islam, M. S., Wang, S., Hao, J., Zhang, H., He, C.,

646   Guo, H., Fu, H., Miljevic, B., Morawska, L., Thai, P., LAM, Y. F., Pereira, G., Ding, A., Huang, X.

647   and Dumka, U. C.: A review of biomass burning: Emissions and impacts on air quality, health and

648   climate in China, Sci. Total Environ., 579(November 2016), 1000–1034,

649   doi:10.1016/j.scitotenv.2016.11.025, 2017.

650   Cheng, J., Su, J., Cui, T., Li, X., Dong, X., Sun, F., Yang, Y., Tong, D., Zheng, Y., Li, J., Zhang, Q.

651   and He, K.: Dominant role of emission reduction in PM$_{2.5}$ air quality improvement in Beijing during

652   2013-2017: a model-based decomposition analysis, Atmos. Chem. Phys., 19, 6125–6146,

653   doi:10.5194/acp-19-6125-2019, 2019.

654   Elliott, E. M., Yu, Z., Cole, A. S. and Coughlin, J. G.: Isotopic advances in understanding reactive

655   nitrogen deposition and atmospheric processing, Sci. Total Environ., 662, 393–403,

656   doi:10.1016/J.SCITOTENV.2018.12.177, 2019.

657   Felix, J. D. and Elliott, E. M.: Isotopic composition of passively collected nitrogen dioxide emissions:

658   Vehicle, soil and livestock source signatures, Atmos. Environ., 92, 359–366,

659   doi:10.1016/j.atmosenv.2014.04.005, 2014.

660   Felix, J. D., Elliott, E. M. and Shaw, S. L.: Nitrogen Isotopic Composition of Coal-Fired Power Plant

661   NO x : Influence of Emission Controls and Implications for Global Emission Inventories, Environ.

662   Sci. Technol., 46(6), 3528–3535, doi:10.1021/es203355v, 2012.

663   Fibiger, D. L. and Hastings, M. G.: First Measurements of the Nitrogen Isotopic Composition of NO

664   $_x$ from Biomass Burning, Environ. Sci. Technol., 50(21), 11569–11574,

665   doi:10.1021/acs.est.6b03510, 2016.

666   Fountoukis, C. and Nenes, A.: ISORROPIA II: a computationally efficient thermodynamic

667   equilibrium model for K+- Ca2+-Mg2+-NH+ 4 -Na+-SO2− 4 -NO− 3 -Cl−-H2O aerosols, Atmos.

668   Chem. Phys., 7(17), 4639–4659, doi:10.5194/acp-7-4639-2007, 2007.

669   Freyer, H. D.: Seasonal variation of 15N/14N ratios in atmospheric nitrate species, Tellus B, 43(1),

670   30–44, doi:10.1034/j.1600-0889.1991.00003.x, 1991.

671   Freyer, H. D., Kley, D., Volz-Thomas, A. and Kobel, K.: On the interaction of isotopic exchange

672   processes with photochemical reactions in atmospheric oxides of nitrogen, J. Geophys. Res., 98(D8),

673   14791, doi:10.1029/93JD00874, 1993.

674   Goldberg, D. L., Saide, P. E., Lamsal, L. N., de Foy, B., Lu, Z., Woo, J.-H., Kim, Y., Kim, J., Gao,

675   M., Carmichael, G. and Streets, D. G.: A top-down assessment using OMI NO2 suggests an

676   underestimate in the NOx emissions inventory in Seoul, South Korea, during KORUS-AQ, Atmos.

677   Chem. Phys., 19(3), 1801–1818, doi:10.5194/acp-19-1801-2019, 2019.

678   Guha, T., Lin, C. T., Bhattacharya, S. K., Mahajan, A. S., Ou-Yang, C.-F., Lan, Y.-P., Hsu, S. C. and

679   Liang, M.-C.: Isotopic ratios of nitrate in aerosol samples from Mt. Lulin, a high-altitude station in

680   Central Taiwan, Atmos. Environ., 154, 53–69, doi:10.1016/J.ATMOSENV.2017.01.036, 2017.

681   Hallquist, M., Stewart, D. J., Stephenson, S. K. and Anthony Cox, R.: Hydrolysis of N2O5 on sub-

682   micron sulfate aerosols, Phys. Chem. Chem. Phys., 5(16), 3453, doi:10.1039/b301827j, 2003.

683   He, P., Xie, Z., Chi, X., Yu, X., Fan, S., Kang, H., Liu, C. and Zhan, H.: Atmospheric Δ17O(NO3-)

684   reveals nocturnal chemistry dominates nitrate production in Beijing haze, Atmos. Chem. Phys.,

685   18(19), 14465–14476, doi:10.5194/acp-18-14465-2018, 2018.

686   He, P., Xie, Z., Yu, X., Wang, L., Kang, H. and Yue, F.: The observation of isotopic compositions of

687   atmospheric nitrate in Shanghai China and its implication for reactive nitrogen chemistry, Sci. Total

688   Environ., 714, 136727, doi:10.1016/J.SCITOTENV.2020.136727, 2020.

689   Heaton, T. H. E.: $^{15}N/^{14}N$ ratios of NOx from vehicle engines and coal-fired power stations, Tellus B,
690   42(3), 304–307, doi:10.1034/j.1600-0889.1990.00007.x-i1, 1990.

691   Ishino, S., Hattori, S., Savarino, J., Jourdain, B., Preunkert, S., Legrand, M., Caillon, N., Barbero, A.,
692   Kuribayashi, K. and Yoshida, N.: Seasonal variations of triple oxygen isotopic compositions of
693   atmospheric sulfate, nitrate, and ozone at Dumont d'Urville, coastal Antarctica, Atmos. Chem. Phys.,
694   17(5), 3713–3727, doi:10.5194/ACP-17-3713-2017, 2017.

695   Kaiser, J., Hastings, M. G., Houlton, B. Z., Röckmann, T. and Sigman, D. M.: Triple oxygen isotope
696   analysis of nitrate using the denitrifier method and thermal decomposition of N2O, Anal. Chem.,
697   79(2), 599–607, doi:10.1021/ac061022s, 2007.

698   Kamezaki, K., Hattori, S., Iwamoto, Y., Ishino, S., Furutani, H., Miki, Y., Uematsu, M., Miura, K.
699   and Yoshida, N.: Tracing the sources and formation pathways of atmospheric particulate nitrate over
700   the Pacific Ocean using stable isotopes, Atmos. Environ., 209, 152–166,
701   doi:10.1016/J.ATMOSENV.2019.04.026, 2019.

702   Kang, H., Zhu, B., Gao, J., He, Y., Wang, H., Su, J., Pan, C., Zhu, T. and Yu, B.: Potential impacts of
703   cold frontal passage on air quality over the Yangtze River Delta, China, Atmos. Chem. Phys., 19(6),
704   3673–3685, doi:10.5194/acp-19-3673-2019, 2019.

705   Kim, H., Zhang, Q. and Sun, Y.: Measurement report: Characterization of severe spring haze episodes
706   and influences of long-range transport in the Seoul metropolitan area in March 2019, Atmos. Chem.
707   Phys., 20(19), 11527–11550, doi:10.5194/acp-20-11527-2020, 2020a.

708   Kim, H. C., Kim, S., Lee, S.-H., Kim, B.-U. and Lee, P.: Fine-Scale Columnar and Surface NOx
709   Concentrations over South Korea: Comparison of Surface Monitors, TROPOMI, CMAQ and CAPSS
710   Inventory, Atmosphere (Basel)., 11(1), 101, doi:10.3390/atmos11010101, 2020b.

711   Kim, S.-W., Yoon, S.-C., Kim, J. and Kim, S.-Y.: Seasonal and monthly variations of columnar
712   aerosol optical properties over east Asia determined from multi-year MODIS, LIDAR, and
713   AERONET Sun/sky radiometer measurements, Atmos. Environ., 41(8), 1634–1651,
714   doi:10.1016/j.atmosenv.2006.10.044, 2007.

715   Lee, H.-J., Jo, H.-Y., Kim, S.-W., Park, M.-S. and Kim, C.-H.: Impacts of atmospheric vertical
716   structures on transboundary aerosol transport from China to South Korea, Sci. Rep., 9(1), 13040,
717   doi:10.1038/s41598-019-49691-z, 2019.

718 Lelieveld, J., Evans, J. S., Fnais, M., Giannadaki, D. and Pozzer, A.: The contribution of outdoor air

719 pollution sources to premature mortality on a global scale, Nature, 525(7569), 367–371,

720 doi:10.1038/nature15371, 2015.

721 Li, D. and Wang, X.: Nitrogen isotopic signature of soil-released nitric oxide (NO) after fertilizer

722 application, Atmos. Environ., 42(19), 4747–4754, doi:10.1016/j.atmosenv.2008.01.042, 2008.

723 Li, H., Zhang, Q., Zheng, B., Chen, C., Wu, N., Guo, H., Zhang, Y., Zheng, Y., Li, X. and He, K.:

724 Nitrate-driven urban haze pollution during summertime over the North China Plain, Atmos. Chem.

725 Phys., 18(8), 5293–5306, doi:10.5194/acp-18-5293-2018, 2018.

726 Li, J., Zhang, X., Orlando, J., Tyndall, G. and Michalski, G.: Quantifying the nitrogen isotope effects

727 during photochemical equilibrium between NO and NO2: Implications for δ15N in tropospheric

728 reactive nitrogen, Atmos. Chem. Phys., 20(16), 9805–9819, doi:10.5194/acp-20-9805-2020, 2020.

729 Li, J., Davy, P., Harvey, M., Katzman, T., Mitchell, T. and Michalski, G.: Nitrogen isotopes in nitrate

730 aerosols collected in the remote marine boundary layer: Implications for nitrogen isotopic

731 fractionations among atmospheric reactive nitrogen species, Atmos. Environ., 245, 118028,

732 doi:10.1016/j.atmosenv.2020.118028, 2021.

733 Li, Z., Walters, W. W., Hastings, M. G., Zhang, Y., Song, L., Liu, D., Zhang, W., Pan, Y., Fu, P. and

734 Fang, Y.: Nitrate Isotopic Composition in Precipitation at a Chinese Megacity: Seasonal Variations,

735 Atmospheric Processes, and Implications for Sources, Earth Sp. Sci., 6(11), 2200–2213,

736 doi:10.1029/2019EA000759, 2019.

737 Lim, S., Lee, M., Czimczik, C. I., Joo, T., Holden, S., Mouteva, G., Santos, G. M., Xu, X., Walker, J.,

738 Kim, S., Kim, H. S., Kim, S. and Lee, S.: Source signatures from combined isotopic analyses of PM$_{2.5}$

739 carbonaceous and nitrogen aerosols at the peri-urban Taehwa Research Forest, South Korea in

740 summer and fall, Sci. Total Environ., 655, 1505–1514, doi:10.1016/j.scitotenv.2018.11.157, 2019.

741 Lim, S., Yang, X., Lee, M., Li, G., Gao, Y., Shang, X., Zhang, K., Czimczik, C. I., Xu, X., Bae, M.-

742 S., Moon, K.-J. and Jeon, K.: Fossil-driven secondary inorganic PM$_{2.5}$ enhancement in the North

743 China Plain: Evidence from carbon and nitrogen isotopes, Environ. Pollut., 266, 115163,

744 doi:10.1016/J.ENVPOL.2020.115163, 2020.

745 Liu, Z., Gao, W., Yu, Y., Hu, B., Xin, J., Sun, Y., Wang, L., Wang, G., Bi, X., Zhang, G., Xu, H.,

746 Cong, Z., He, J., Xu, J. and Wang, Y.: Characteristics of PM$_{2.5}$ mass concentrations and chemical

747   species in urban and background areas of China: emerging results from the CARE-China network,

748   Atmos. Chem. Phys., 18(12), 8849–8871, doi:10.5194/acp-18-8849-2018, 2018.

749   McIlvin, M. R. and Casciotti, K. L.: Technical updates to the bacterial method for nitrate isotopic

750   analyses, Anal. Chem., 83(5), 1850–1856, doi:10.1021/AC1028984, 2011.

751   Michalski, G. and Bhattacharya, S. K.: The role of symmetry in the mass independent isotope effect in

752   ozone, Proc. Natl. Acad. Sci., 106(14), 5493–5496, doi:10.1073/PNAS.0812755106, 2009.

753   Michalski, G., Scott, Z., Kabiling, M. and Thiemens, M. H.: First measurements and modeling of Δ^{17}

754   O in atmospheric nitrate, Geophys. Res. Lett., 30(16), doi:10.1029/2003GL017015, 2003.

755   Michalski, G., Meixner, T., Fenn, M., Hernandez, L., Sirulnik, A., Edith Allen, A. and Thiemens†,

756   M.: Tracing Atmospheric Nitrate Deposition in a Complex Semiarid Ecosystem Using $\Delta17O$, ,

757   doi:10.1021/ES034980+, 2004.

758   Morin, S., Savarino, J., Frey, M. M., Domine, F., Jacobi, H.-W., Kaleschke, L. and Martins, J. M. F.:

759   Comprehensive isotopic composition of atmospheric nitrate in the Atlantic Ocean boundary layer

760   from 65°S to 79°N, J. Geophys. Res., 114(D5), D05303, doi:10.1029/2008JD010696, 2009.

761   Morin, S., Sander, R. and Savarino, J.: Simulation of the diurnal variations of the oxygen isotope

762   anomaly (Δ 17 O) of reactive atmospheric species, Atmos. Chem. Phys., 11(8), 3653–3671,

763   doi:10.5194/acp-11-3653-2011, 2011.

764   Nelson, D. M., Tsunogai, U., Ding, D., Ohyama, T., Komatsu, D. D., Nakagawa, F., Noguchi, I. and

765   Yamaguchi, T.: Triple oxygen isotopes indicate urbanization affects sources of nitrate in wet and dry

766   atmospheric deposition, Atmos. Chem. Phys., 18(9), 6381–6392, doi:10.5194/acp-18-6381-2018,

767   2018.

768   Park, Y., Park, K., Kim, H., Yu, S., Noh, S., Kim, M., Kim, J., Ahn, J., Lee, M., Seok, K. and Kim,

769   Y.: Characterizing isotopic compositions of TC-C, NO_3^--N, and NH_4^+-N in $PM_{2.5}$ in South Korea:

770   Impact of China's winter heating, Environ. Pollut., 233, 735–744,

771   doi:10.1016/J.ENVPOL.2017.10.072, 2018.

772   Parnell, A. C., Inger, R., Bearhop, S. and Jackson, A. L.: Source Partitioning Using Stable Isotopes:

773   Coping with Too Much Variation, edited by S. Rands, PLoS One, 5(3), e9672,

774   doi:10.1371/journal.pone.0009672, 2010.

775 Parnell, A. C., Phillips, D. L., Bearhop, S., Semmens, B. X., Ward, E. J., Moore, J. W., Jackson, A.

776 L., Grey, J., Kelly, D. J. and Inger, R.: Bayesian stable isotope mixing models, Environmetrics, 24(6),

777 387–399, doi:10.1002/env.2221, 2013.

778 Quan, J., Dou, Y., Zhao, X., Liu, Q., Sun, Z., Pan, Y., Jia, X., Cheng, Z., Ma, P., Su, J., Xin, J. and

779 Liu, Y.: Regional atmospheric pollutant transport mechanisms over the North China Plain driven by

780 topography and planetary boundary layer processes, Atmos. Environ., 221, 117098,

781 doi:10.1016/J.ATMOSENV.2019.117098, 2020.

782 Rose, L. A., Yu, Z., Bain, D. J. and Elliott, E. M.: High resolution, extreme isotopic variability of

783 precipitation nitrate, Atmos. Environ., 207, 63–74, doi:10.1016/J.ATMOSENV.2019.03.012, 2019.

784 Saunders, S. M., Jenkin, M. E., Derwent, R. G. and Pilling, M. J.: Protocol for the development of the

785 Master Chemical Mechanism, MCM v3 (Part A): Tropospheric degradation of non-aromatic volatile

786 organic compounds, Atmos. Chem. Phys., 3(1), 161–180, doi:10.5194/acp-3-161-2003, 2003.

787 Savarino, J., Kaiser, J., Morin, S., Sigman, D. M. and Thiemens, M. H.: Nitrogen and oxygen isotopic

788 constraints on the origin of atmospheric nitrate in coastal Antarctica, Atmos. Chem. Phys., 7(8),

789 1925–1945, doi:10.5194/acp-7-1925-2007, 2007.

790 Savarino, J., Morin, S., Erbland, J., Grannec, F., Patey, M. D., Vicars, W., Alexander, B. and

791 Achterberg, E. P.: Isotopic composition of atmospheric nitrate in a tropical marine boundary layer.,

792 Proc. Natl. Acad. Sci. U. S. A., 110(44), 17668–73, doi:10.1073/pnas.1216639110, 2013.

793 Shao, P., Tian, H., Sun, Y., Liu, H., Wu, B., Liu, S., Liu, X., Wu, Y., Liang, W., Wang, Y., Gao, J.,

794 Xue, Y., Bai, X., Liu, W., Lin, S. and Hu, G.: Characterizing remarkable changes of severe haze

795 events and chemical compositions in multi-size airborne particles (PM_1, $PM_{2.5}$ and PM_{10}) from

796 January 2013 to 2016–2017 winter in Beijing, China, Atmos. Environ., 189, 133–144,

797 doi:10.1016/J.ATMOSENV.2018.06.038, 2018.

798 Sharma, H. D., Jervis, R. E. and Wong, K. Y.: Isotopic exchange reactions in nitrogen oxides, J. Phys.

799 Chem., 74(4), 923–933, doi:10.1021/j100699a044, 1970.

800 Shi, C., Nduka, I. C., Yang, Y., Huang, Y., Yao, R., Zhang, H., He, B., Xie, C., Wang, Z. and Yim, S.

801 H. L.: Characteristics and meteorological mechanisms of transboundary air pollution in a persistent

802 heavy $PM_{2.5}$ pollution episode in Central-East China, Atmos. Environ., 223, 117239,

803 doi:10.1016/J.ATMOSENV.2019.117239, 2020.

804 Song, W., Wang, Y.-L., Yang, W., Sun, X.-C., Tong, Y.-D., Wang, X.-M., Liu, C.-Q., Bai, Z.-P. and
805 Liu, X.-Y.: Isotopic evaluation on relative contributions of major NOx sources to nitrate of $PM_{2.5}$ in
806 Beijing, Environ. Pollut., 248, 183–190, doi:10.1016/J.ENVPOL.2019.01.081, 2019.

807 Song, W., Liu, X.-Y., Wang, Y.-L., Tong, Y.-D., Bai, Z.-P. and Liu, C.-Q.: Nitrogen isotope
808 differences between atmospheric nitrate and corresponding nitrogen oxides: A new constraint using
809 oxygen isotopes, Sci. Total Environ., 701, 134515, doi:10.1016/J.SCITOTENV.2019.134515, 2020.

810 Stein, A. F., Draxler, R. R., Rolph, G. D., Stunder, B. J. B., Cohen, M. D. and Ngan, F.: NOAA's
811 HYSPLIT Atmospheric Transport and Dispersion Modeling System, Bull. Am. Meteorol. Soc.,
812 96(12), 2059–2077, doi:10.1175/BAMS-D-14-00110.1, 2015.

813 Thiemens, M. H.: Mass-independent isotope effects in planetary atmospheres and the early solar
814 system, Science (80-.)., 283(5400), 341–345, doi:10.1126/science.283.5400.341, 1999.

815 Thiemens, M. H.: HISTORY AND APPLICATIONS OF MASS-INDEPENDENT ISOTOPE
816 EFFECTS, Annu. Rev. Earth Planet. Sci., 34(1), 217–262,
817 doi:10.1146/annurev.earth.34.031405.125026, 2006.

818 Tong, D., Zhang, Q., Liu, F., Geng, G., Zheng, Y., Xue, T., Hong, C., Wu, R., Qin, Y., Zhao, H., Yan,
819 L. and He, K.: Current Emissions and Future Mitigation Pathways of Coal-Fired Power Plants in
820 China from 2010 to 2030, Environ. Sci. Technol., 52(21), 12905–12914, doi:10.1021/acs.est.8b02919,
821 2018.

822 Vicars, W. C. and Savarino, J.: Quantitative constraints on the ^{17}O-excess ($\Delta^{17}O$) signature of surface
823 ozone: Ambient measurements from 50°N to 50°S using the nitrite-coated filter technique, Geochim.
824 Cosmochim. Acta, 135, 270–287, doi:10.1016/J.GCA.2014.03.023, 2014.

825 Vicars, W. C., Bhattacharya, S. K., Erbland, J. and Savarino, J.: Measurement of the ^{17}O-excess
826 ($\Delta^{17}O$) of tropospheric ozone using a nitrite-coated filter, Rapid Commun. Mass Spectrom., 26(10),
827 1219–1231, doi:10.1002/rcm.6218, 2012.

828 Wahner, A., Mentel, T. F., Sohn, M. and Stier, J.: Heterogeneous reaction of N_2O_5 on sodium nitrate
829 aerosol, J. Geophys. Res. Atmos., 103(D23), 31103–31112, doi:10.1029/1998JD100022, 1998.

830 Walters, W. W. and Michalski, G.: Theoretical calculation of nitrogen isotope equilibrium exchange
831 fractionation factors for various NO_y molecules, Geochim. Cosmochim. Acta, 164, 284–297,
832 doi:10.1016/J.GCA.2015.05.029, 2015.

833   Walters, W. W. and Michalski, G.: Theoretical calculation of oxygen equilibrium isotope

834   fractionation factors involving various NO molecules, OH, and H_2O and its implications for isotope

835   variations in atmospheric nitrate, Geochim. Cosmochim. Acta, 191, 89–101,

836   doi:10.1016/j.gca.2016.06.039, 2016.

837   Walters, W. W., Goodwin, S. R. and Michalski, G.: Nitrogen Stable Isotope Composition ($\delta^{15}N$) of

838   Vehicle-Emitted NO_x, Environ. Sci. Technol., 49(4), 2278–2285, doi:10.1021/es505580v, 2015.

839   Walters, W. W., Simonini, D. S. and Michalski, G.: Nitrogen isotope exchange between NO and NO_2

840   and its implications for $\delta^{15}N$ variations in tropospheric NO_x and atmospheric nitrate, Geophys. Res.

841   Lett., 43(1), 440–448, doi:10.1002/2015GL066438, 2016.

842   Walters, W. W., Fang, H. and Michalski, G.: Summertime diurnal variations in the isotopic

843   composition of atmospheric nitrogen dioxide at a small midwestern United States city, Atmos.

844   Environ., 179, 1–11, doi:10.1016/J.ATMOSENV.2018.01.047, 2018.

845   Wang, Y., Wang, Y., Wang, L., Petäjä, T., Zha, Q., Gong, C., Li, S., Pan, Y., Hu, B., Xin, J. and

846   Kulmala, M.: Increased inorganic aerosol fraction contributes to air pollution and haze in China,

847   Atmos. Chem. Phys., 19(9), 5881–5888, doi:10.5194/acp-19-5881-2019, 2019a.

848   Wang, Y., Song, W., Yang, W., Sun, X., Tong, Y., Wang, X., Liu, C., Bai, Z. and Liu, X.: Influences

849   of Atmospheric Pollution on the Contributions of Major Oxidation Pathways to PM $_{2.5}$ Nitrate

850   Formation in Beijing, J. Geophys. Res. Atmos., 124(7), 4174–4185, doi:10.1029/2019JD030284,

851   2019b.

852   van der Werf, G. R., Randerson, J. T., Giglio, L., Collatz, G. J., Mu, M., Kasibhatla, P. S., Morton, D.

853   C., DeFries, R. S., Jin, Y. and van Leeuwen, T. T.: Global fire emissions and the contribution of

854   deforestation, savanna, forest, agricultural, and peat fires (1997–2009), Atmos. Chem. Phys., 10(23),

855   11707–11735, doi:10.5194/acp-10-11707-2010, 2010.

856   Xie, Y., Dai, H., Zhang, Y., Wu, Y., Hanaoka, T. and Masui, T.: Comparison of health and economic

857   impacts of $PM_{2.5}$ and ozone pollution in China, Environ. Int., 130, 104881,

858   doi:10.1016/J.ENVINT.2019.05.075, 2019.

859   Xu, W., Sun, Y., Wang, Q., Zhao, J., Wang, J., Ge, X., Xie, C., Zhou, W., Du, W., Li, J., Fu, P.,

860   Wang, Z., Worsnop, D. R. and Coe, H.: Changes in Aerosol Chemistry From 2014 to 2016 in Winter

861   in Beijing: Insights From High-Resolution Aerosol Mass Spectrometry, J. Geophys. Res. Atmos.,

862   124(2), 1132–1147, doi:10.1029/2018JD029245, 2019.

863   Yu, Z. and Elliott, E. M.: Novel method for nitrogen isotopic analysis of soil-emitted nitric oxide,

864   Environ. Sci. Technol., 51(11), 6268–6278, doi:10.1021/acs.est.7b00592, 2017.

865   Zhao, H., Zhang, X., Zhang, S., Chen, W., Tong, D., Xiu, A., Zhao, H., Zhang, X., Zhang, S., Chen,

866   W., Tong, D. Q. and Xiu, A.: Effects of Agricultural Biomass Burning on Regional Haze in China: A

867   Review, Atmosphere (Basel)., 8(12), 88, doi:10.3390/atmos8050088, 2017.

868   Zheng, H., Kong, S., Wu, F., Cheng, Y., Niu, Z., Zheng, S., Yang, G., Yao, L., Yan, Q., Wu, J.,

869   Zheng, M., Chen, N., Xu, K., Yan, Y., Liu, D., Zhao, D., Zhao, T., Bai, Y., Li, S. and Qi, S.: Intra-

870   regional transport of black carbon between the south edge of the North China Plain and central China

871   during winter haze episodes, Atmos. Chem. Phys., 19(7), 4499–4516, doi:10.5194/acp-19-4499-2019,

872   2019.

873   Zong, Z., Wang, X., Tian, C., Chen, Y., Fang, Y., Zhang, F., Li, C., Sun, J., Li, J. and Zhang, G.: First

874   assessment of NO_x sources at a regional background site in north China using isotopic analysis linked

875   with modeling, Environ. Sci. Technol., 51(11), 5923–5931, doi:10.1021/acs.est.6b06316, 2017.

876   Zong, Z., Tan, Y., Wang, X., Tian, C., Li, J., Fang, Y., Chen, Y., Cui, S. and Zhang, G.: Dual-

877   modelling-based source apportionment of NOx in five Chinese megacities: Providing the isotopic

878   footprint from 2013 to 2014, Environ. Int., 137, 105592, doi:10.1016/J.ENVINT.2020.105592, 2020.

879